Instituto Tecnológico y de Estudios Superiores de Occidente

Reconocimiento de validez oficial de estudios de nivel superior según acuerdo secretarial 15018, publicado en el Diario Oficial de la Federación del 29 de noviembre de 1976.

Departamento de Electrónica, Sistemas e Informática

Master's in Computer Systems

Multispectral Image Analysis of Remotely Sensed Crops

TRABAJO RECEPCIONAL que para obtener el GRADO de MAESTRO EN SISTEMAS COMPUTACIONALES

Author: **JOSÉ DE JESÚS VILLANUEVA MOLINA**

Advisor: **DR. ALBERTO DE OBESO ORENDAIN**

Tlaquepaque, Jalisco. Mayo de 2022.

Dedications and Acknowledgments

First and foremost, I would like to thank my parents, Gabriela Molina Acuña and Jose de Jesus Villanueva Olivera, and sister Rubi Villanueva Molina, whose support has been crucial for this thesis. I would not be standing where I am today without your infinite love, wisdom, and support. Thanks for always believing in me and giving me the strength to follow my dreams. At the same time, my thanks also go to Jessica Cisneros Gonzalez for cheering me up when times got challenging.

I thank my adviser, Dr. Alberto de Obeso, for his unwavering support, encouragement, and patience through this educational process. Thank you for being the link between me, Precisión Agrícola, the University of Guadalajara, and ITESO. For your patience, time, and advice.

Last but not least, I would like to thank CONACYT for the economic scholarship with number 503287 throughout these two years. The support allowed me to continue my academic formation, providing resources and facilities to complete the research.

Abstract

The range in topography, biodiversity, and agricultural technology has led to the emergence of precision agriculture. Precision agriculture is a farming management concept based on monitoring, measuring, and responding to crop variability. Computer vision, image analysis, and image processing are gaining considerable traction.

For this paper, image analysis involves recognizing individual objects and providing insights from vegetation indices. The data acquired was remote-sensed multispectral images from blueberry, maguey, and pineapple. After computing vegetation indices, histograms were analyzed to choose thresholds. The masking of vegetation indices with threshold allowed the removal of areas with shadows and soil. The four leading vegetation indices used were the Normalized Difference Vegetation Index (NDVI), the Normalized Difference Red Edge (NDRE), the Simple Ratio, the Red Edge Chlorophyll Index, and the Visible Atmospherically Resistant Index (SAVI).

This research reviews literature for acquiring, preprocessing, and analyzing remote-sensed multispectral images in precision agriculture. It compiles the theoretical framework for analyzing multispectral data. Also, it describes and implements radiometric calibration and image alignment using the custom code from the MicaSense repository.

As a result, it was possible to segment the blueberry, tequila agave, and pineapple plants from the background regardless of the noisy images. Non-plant pixels were excluded and shown as transparent by masking areas with shadows and low NDVI pixels, which sometimes removed plant pixels. The NDVI and NDRE helped identify crop pixels. On the other hand, it was possible to identify the pineapple fruits from the agave plantation using the SAVI vegetation index and the thresholding method. Finally, the work identifies the problems associated with an incorrect data acquisition methodology and provides suggestions.

0. TABLE OF CONTENT

1. INTRODUCTION

1.1 Background

The range in topography, biodiversity, and agricultural technology has led to the emergence of precision agriculture. The USA National Research Council defines it as “a management strategy that uses information technology to bring data from multiple sources to bear on decisions associated with crop production.”[1] The concept promises increasing productivity while decreasing production costs and minimizing environmental impacts. The data collected is mainly on the stage and health of crops to then mapping features associated with harvestability and yield.

In precision agriculture, computer vision, image analysis, and image processing are gaining considerable traction. Applications include fruit and plant detection, grading and counting fruits, leaf disease detection, quality characterization, crop yield prediction, and field inspection. However, there are no clear boundaries among researchers between the three areas. For this paper, image analysis involves recognizing individual objects and providing valuable insights from images. [2] The complexity level depends on the selected path to find insights, such as machine learning algorithms, statistical methods, and more straightforward mathematical calculations. On the other hand, remotely sensing alludes to obtaining information about objects or areas without being invasive or destructive.[3] Typically, raw images come from satellites, Unmanned Aerial Systems (UAS), LiDARs, webcams, or smartphones.

1.2 Hypothesis

The data acquisition and image processing methodologies affect the analysis of multispectral images.

1.3 Objectives

This research reviews literature for acquiring, processing, and analyzing remote-sensed multispectral images in precision agriculture. Open-source tools were critical for processing and analyzing images, mainly the MicaSense repository. The data acquired was remote-sensed multispectral images from several crops, such as blueberry, maguey, and pineapple. The studied crops have a high market share in Mexico´s agriculture production and exports. The research focuses on three main objectives:

1) Review literature on remotely sensed images in precision agriculture.
2) Create a theoretical framework for acquiring, processing, and analyzing multispectral images.
3) Using open-source tools, implement a methodology to process and analyze multispectral images using vegetation indices.

2. STATE OF ART

2.1 Fundamental Concepts

Researchers have no general agreement regarding clear-cut boundaries between image processing, image analysis, and computer vision.

In the book *Computer Vision and Image Processing: Fundamentals and Applications*, Ph.D. Manas Jamal Bhuyan summarizes the differences. In the 2020 edition, Professor Jamal Bhuyan distinguishes image processing as a discipline in which the input and output are images. Moreover, he defines computer vision as a field in computer science in which the input is an image, and the output is an interpretation. He also establishes computer vision, image analysis, image interpretation, and scene understanding as synonyms. [4]

In the book *Digital Image Processing*, Ph.D. Rafael C. Gonzalez and Ph.D. Richard E. In the 2018 edition, Woods states that the previous definitions are limiting and artificial. Richard and Rafael argue that, under these definitions, computing an image's average intensity would not be considered an image processing operation. [5] Henceforth, they propose considering the three types of computerized processes in the continuum: low-, mid-, and high-level.

- **In the low-level process**, inputs and outputs are images. It addresses operations such as image preprocessing to crop, resize, contrast enhance, filter noise, morphological operations, and color model conversions. [6] The goal is to prepare images to gain better results for later analysis. Researchers compensate for sensor characteristics and light and atmospheric conditions during this step.
- **In the mid-level process**, inputs are images, and outputs are attributes extracted from the images. The most common attributes (also known as features) are color, contours, edges, shape, texture, and the identity of individual objects. Mid-level processing involves segmentation, description of objects, and classification (recognition) of individual objects. Image segmentation consists of grouping pixels according to specific features of the object to recognize.[7] It intends to isolate the Return of Investment (ROI) from an image's non-interesting pixels.

- **In the high-level process**, outputs are insights of recognized objects. Making sense of the objects is both in the domain of image analysis and computer vision. These can be biomass calculation and fruit counting in precision agriculture.

From the previous paradigm shift, image processing and image analysis overlap in the area of recognition of individual regions or objects in an image. On the other hand, computer vision and image analysis overlap in "making sense" of the recognized objects.

For this paper, image analysis involves recognizing individual objects and providing insights from an image. The complexity level depends on the selected path to find insights, such as machine learning algorithms, statistical methods, and more straightforward mathematical calculations.

2.2 Image Sources in Precision Agriculture

Raw images come from mainly four image sources: RGB (Red, Green, and Blue), Three-dimensional, hyperspectral, and multispectral cameras. Critical factors for selecting the right equipment include (a) camera's sensor resolution; (b) budget; (c) type of image sensors; (d) frame rate; and (e) image transfer rate. [8] The equipment for image acquisition also depends on the aim of the study and the resources available for researchers.

The most cost-effective applications use the RGB channels. Image acquisition typically relies on digital or built-in cameras of mobile devices. An adequate mathematical representation of color is critical for processing the features of color independently.[5] The essential features are intensity and chromaticity. Regarding the color space, the RGB color space is less desirable for color processing because intensity and chromaticity are not decoupled. [9] Another reason is the high correlation between the red, green, and blue channels. Therefore, color model conversion or implementing advanced algorithms are essential for image analysis.[6] For instance, Pushkara Sharma, Pankaj Hans, and Subhash Chand converted their images from RGB to HSV color space because HSV separates color from intensity. [10] Then, they applied K-means clustering to separate the leaves from the background.

In crop and plant monitoring and species discrimination applications, 3D images from stereoscopic cameras are helpful. This data source provides additional crop dimensions, such as depth information, crop height, and leaf shape. However, they have had less accuracy in

comparison with other data sources. Daeun Choi and Won Suk Lee analyzed the performance of RGB, NIR, and depth images for immature citrus fruit detection using machine vision techniques. [11] Choi and Lee conducted a performance comparison based on: 1) circular object detection to find potential fruit areas and 2) classifying citrus fruit from the background using deep learning. They applied circular Hough transform in the RGB and NIR images for circular object detection. On the other hand, they developed a new CHOI's Circle Estimation (CHOICE) algorithm to detect spherical objects for depth images. The CHOICE algorithm uses divergence and vorticity in a gradient vector field. The results showed that the NIR images had a 96% accuracy performance, contrasting with the 91.6% RGB images. The depth images had the worst performance, with 90.3% accuracy.[11]

The remote sensing industry differentiates between multispectral and hyperspectral equipment based on the number of spectral bands. Multispectral sensors commonly capture less than ten bands. Hyperspectral sensors usually have bands in hundreds, so they capture more information than digital color and multispectral cameras. A drawback is that hyperspectral images contain redundancy since adjacent bands in the electromagnetic (EM) spectrum tend to have similar data. [12] Another disadvantage is that some bands are useless for classifying objects.

Studies have been focusing on the feasibility of hyperspectral imagery in precision agriculture. In 2012, Ce Yang and Won Suk Lee analyzed the spectral signature of blueberry leaves, mature fruits, intermediate fruits, and young fruits. They measured the spectral reflectance in the 200–2500 nm with an increment of 1 nm. Yang and Lee used normalized indices for classification. Each index was composed of the two wavelengths with the most significant reflectance difference between the two classes. Their model of the five-class blueberry classification yielded very high prediction accuracy. [13] In follow-up research, Ce Yang, Won Suk Lee, and Han Li explored the feasibility of hyperspectral imagery for classifying background and blueberries of different growth stages. Figure 1 shows that mature berries have low reflectance in visible and NIR (717 nm) wavelengths. Intermediate berries have lower reflectance than young fruit in the green (560 nm) wavelength but higher reflectance in the red (668 nm) and NIR channels. They proposed a band selection method

using normalized histograms of classes to calculate the KullbackLeibler divergence (KLD). The wavelengths with the largest KLDs between every two classes were selected.[12]

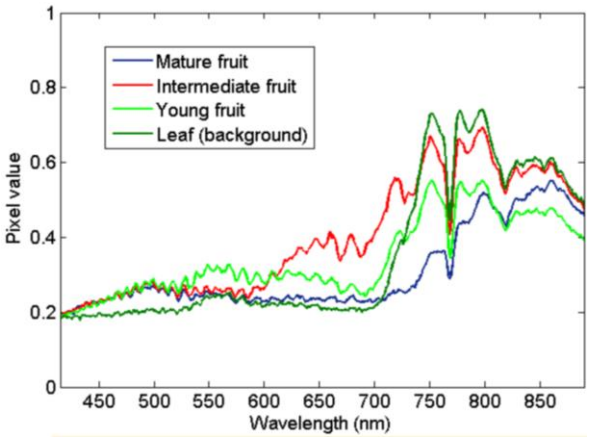

Figure 1 Spectral Signature of Four Pixels

Multispectral sensors capture visible and near-infrared (VNIR) bands. They commonly include the red (R), green (G), blue (B), red-edge (rEdge), and near-infrared (NIR) channels. Some even extend into the thermal spectral range. Understanding the spectral behavior of features of selected objects in different bands is essential for multispectral image analysis. The spectral signature shows the amount of energy reflected in a particular wavelength. Long Qi, Xu Ma, Yanjun Zum, Xianglong Liao, and Hongjiang Guo exploited the spectral signatures of rice seedlings to segment them from the paddy field's background.[14] They calculated the Difference Vegetation Index (DVI) to reduce noise and highlight seedlings. Then, they implemented the fuzzy c-means clustering method to dynamically set the image segmentation threshold according to the DVI image's characteristics. The results showed an accuracy of segmentation of above 99%. Moreover, the spectral response also allows estimating objects' chemical and physical properties. Since growth state, stress levels, and plant vigor directly affect the plant´s reflected light. It helps determine crops' health status and soil properties by calculating the vegetation indices.[15]

2.3 Applications and Challenges in Precision Agriculture

Crop segmentation from the background is critical in precision agriculture. Applications include estimating the crops' fitness and monitoring plant diseases and insect pests [14]. Nonetheless, the segmentation process has its challenges. Variable outdoor lighting conditions induce changes in color features, leading to misclassification. Color space

transformation and the application of advanced algorithms are solutions at the expense of processing speed and increased complexity. Sajad Sabzia, Yousef Abbaspour-Gilandeha, and Hossein Javadikiab suggested a machine vision system based on a hybrid artificial neural network-harmony search (ANN-HS) classifiers. The system segments plants in different growth stages under different lighting conditions. [16] For classification, the authors selected five features among 126 extracting features of five color spaces: CMY (Cyan, Magenta, Yellow), HIS (Hue, Saturation, and Intensity), HSV (Hue, Saturation, and Value), YIQ (Intensity and Color information), and YCbCr.

The health of plants and fruits is a concern for farmers. Reduction in production loss and crop damages can affect marketable yields. The most important facts to monitor the health of plants and fruits are weeds, insects, and diseases. In 2019, Alvaro Irias Tejeda and Rigo Castro proposed an algorithm that detects weed through binary classification.[17] The algorithm detects weeds between the plants inside and outside the crop lines. Nonetheless, it loses effectiveness when the sizes of the weeds are like the sizes of plants. In 2021, A. Lakshmanarao, M. Raja Babu, and T. Srinivasa Ravi Kiran applied Convolutional Neural Networks (Convnets) for plant disease detection to a PlantVillage dataset from Kaggle. The dataset comprises 15 categories of plant leaf images of three types of potato leaves, two types of pepper leaves, and ten types of tomato leaves. The authors achieved an accuracy of 98.3%, 98.5%, and 94% for potato disease detection, pepper bell disease detection, and tomato disease detection, respectively.[18]

Fruit identification leverages image segmentation techniques for locating fruit from crops and the background. Juntao Deng and Zinje Niu compared random forests, support vector machines, and convolutional networks for segmenting kiwifruit vines from orthophotos images. [19] The results show an accuracy of 72.6% for random forests, 85.8% for the support vector machine, and 71.2% for deep semantic segmentation with the same dataset. However, shape irregularity, multiple sizes, and complex backgrounds make it hard to detect fruits.[8] Examples of complex backgrounds include hidden fruit in foliage and branches and similar color variants between the fruits and their background. Subhajit Sengupta and Won Suk Lee developed an algorithm to detect immature green Citrus within a green canopy under natural outdoor conditions. The proposed system uses shape analysis to detect fruits. Then,

Sengupta and Lee remove false positives based on texture classification and Hough line and Canny edge detection. Next, they detected Citrus using a scale-invariant feature transform algorithm for further removal of false positives. The algorithm accurately detected and count 80.4% of citrus fruits under natural outdoor conditions. [20]

Harvesting involves gathering ripe crops and fruits from fields. Manual counting and sorting of fruits are labor-intensive tasks, which lead to errors due to human involvement and variability in the quality of products.[8] While fruit counting allows for estimating yield, fruit grading refers to sorting fruit based on size, shape, and maturity level. Recent studies have focused on automating fruit counting and sorting. Xueping Ni, Changying Li, Huanyu Jiang, and Fumiomi Takeda proposed an approach for counting berries per cluster, measuring maturity, and evaluating cluster tightness. [21] They applied the Mask R-CNN model for segmenting individual blueberries, assessing individual fruit maturity, and cluster maturity indexes. The dataset contained outdoor color images of four southern highbush blueberry cultivars: Emerald, Farthing, Meadowlark, and Star. The mean average precision (mAP) for the validation and test dataset was 78.3% and 71.6% under the 0.5 intersection over union (IOU) threshold. Moreover, their accuracy was 90.6% and 90.4%, respectively.

3. THEORETICAL FRAMEWORK

In remote sensing, sensors mounted on an aircraft or spacecraft platform capture the energy from the earth's surface. Objects reflected light is often in the sun´s visible and non-visible electromagnetic (EM) spectrum. Typically, sensors capture wavelengths from 400 to 2500 nm, then construct an image based on the reflected energy. Spatially, an image is composed of discrete picture elements, known as pixels. Radiometrically, an image quantizes brightness into discrete values.

A remotely sensed image's most significant technical characteristics are the wavelengths, the number of spectral bands, spatial resolution, and radiometric resolution. Chapter 3 reviews the critical properties of multispectral image data.

3.1 Spectral Bands

Sensors measure emanating energy (radiation) at specific ranges of the EM spectrum, called spectral bands. Spectral bands, also known as bands or channels, refer to the location and bandwidth of the sensors´ spectral measurements.[22] For instance, visible light contains blue, green, and red bands ranging between 380 and 780 nanometers (nm) wavelengths. Additionally, spectral resolution refers to the number and location in the EM of spectral bands on a given remote sensing device. [2]

In the remote sensing industry, multispectral cameras have a spectral resolution between three and ten spectral bands in the VIR spectrum range. The red, green, blue, near-infrared, and red-edge bands might be sufficient for information extraction processes such as plant and fruit segmentation and impervious surfaces. Table 1 shows the spectral bands, center wavelength, and bandwidth for the RedEdge-P Micasense Multispectral camera.[22]

Spectral Band	Abbreviation	Center Wavelength (nm)	Bandwidth (nm)
Blue	B	475	32
Green	G	560	27
Red	R	668	14
Red Edge	rEdge	717	12
Near InfraRed	NIR	842	57

Table 1 Spectral Resolution of the RedEdge-P Multispectral Camera

Figure 2 shows the spectral resolution of the Micasense RedEdge-P camera.

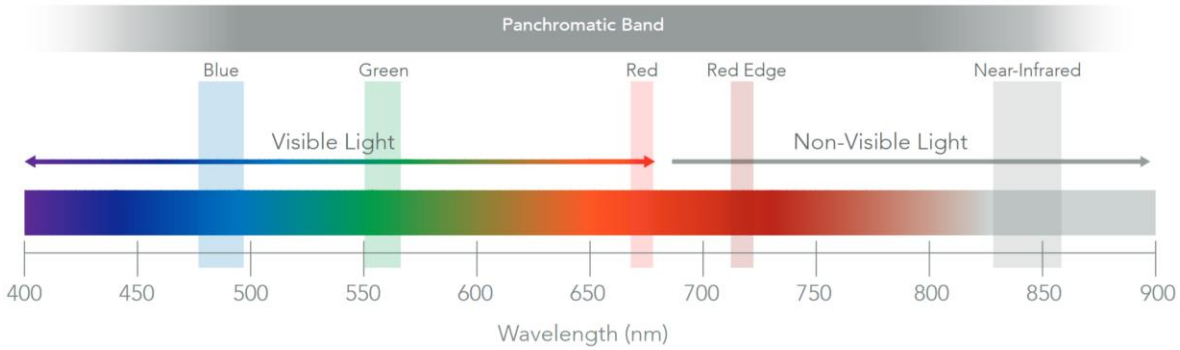

Figure 2 Spectral Resolution of MicaSense RedEdge-P Sensors

3.2 Spatial Resolution

Spatial resolution refers to the area covered on the ground by a single pixel, also known as pixel size.[2] It expresses the ground sampling distance (GSD), and the standard units are meters. Spatial resolution depends on various factors, as shown in Figure 3. The sensor field of view (FOV) is the angular extent of the view the sensor has across the earth's surface; its unit is degrees. Similarly, the instantaneous field of view (IFOV) is the ground area sensed for a pixel at a given instant of time; its unit is m*rad.[23] The swath width (also known as frame size) refers to the kilometers the recorded image covers. [22] Finally, the sensor's altitude affects the FOV, IFOV, and swath width.

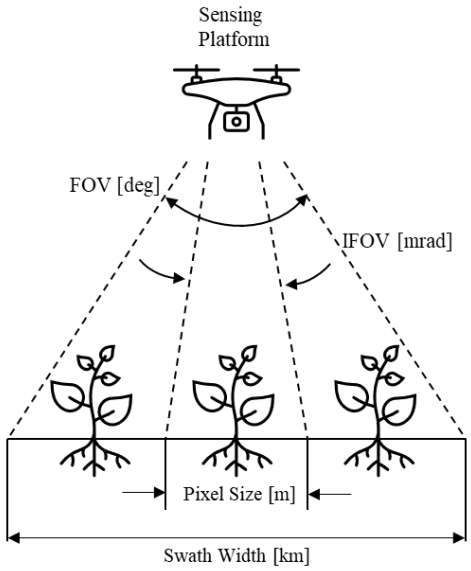

Figure 3 Image Spatial Properties

Spatial resolution plays a vital role in identifying objects using remote sensing imagery. As pixel size decreases, images preserve more details and file size increases. In the book Multispectral Image Analysis Using the Object-Oriented Paradigm, author Kumar Navulur provides rough guidelines for definitions of spatial resolutions. Table 2 shows the guidelines for spatial resolution.

Resolution	**Lower Limit GSD (m)**	**Upper Limit GSD (m)**	**File Size (kb)**
Low	30	> 30	4
Medium	2.0	30	625 - 17
High	0.5	2.0	10851 - 625
Very High	0.15	0.5	173611 - 10851

Table 2 Guidelines of Spatial Resolution

Platform	Spatial Resolution	Field of View	Data Acquisition Cost
UAV	0.5 – 10 cm	50 – 500 m	Very Low
Helicopter	5 – 50 cm	0.2 – 2 km	Medium
Airborne	0.1 – 2 m	0.5 – 5 km	High
Satellite	1 – 25 m	10 – 50 km	Very High

Table 3 Comparison of Data Acquisition Platforms

Imagining in remote sensing can be carried out from aircraft and satellite platforms. Typical examples include Unmanned Aerial Vehicles (UAVs), helicopters, airborne, and satellites.

In many ways, they capture images with similar characteristics. However, altitude and sensor technology differences can lead to differing image properties. In 2015, Sebastian Candiago and Fabio Remondino created a table to compare and contrast remote sensing platforms. [24] Candiago and Remondino found that UAVs have a better spatial and temporal resolution and lower costs than other aircraft and satellite platforms, as shown in Table 3.

3.3 Radiometric Resolution

In remote sensing, sensors capture the electromagnetic radiation of a relatively small area at every pixel location. Spectral radiance records the electromagnetic radiation at certain spectral bands, describing the power density of radiation per unit source area, IFOV angle, and unit wavelength. [25] It has the units of W*m-2*sr-1*um-1, where sr stands for steradian.

Sensors convert the radiance their detectors see at each pixel into an analog signal. Then, detectors convert analog signals to brightness level values through a process referred to as analog-to-digital conversion. Radiometric resolution describes a range of available brightness values recorded for a pixel. It expresses the digital numbers (DN) or bits necessary to represent the range of available brightness values, as shown in Figure 4.

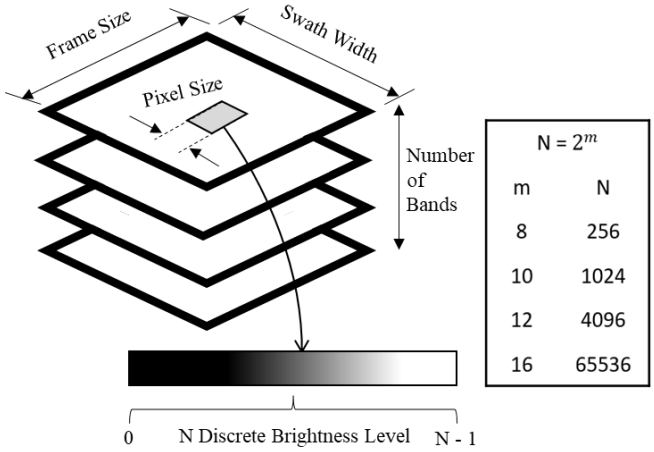

Figure 4 Radiometric Resolution of Images

The pixel DN values are affected by the spectral response of objects, ground spatial resolution, feature size, neighboring features, and more. Radiometric depth or dynamic range are alternative names. For example, data with the 8-bit radiometric resolution has 256

levels of brightness, from 0 to 255. Data with the 12-bit radiometric resolution has 4096 brightness levels, from 0 to 4095.

The equation to compute the radiometric resolution is:

$$N = 2^m,$$

where N is the DN value range and m is the radiometric depth.

The higher the radiometric resolution, the more information content is captured in each spectral band. Standard multispectral imagery formats store data in increments of 8 bits. It is worth mentioning that sensors store 11-bit or 12-bit radiometric resolution images in 16-bit format with empty bits packed at the end.

3.4 Radiometric Calibration

The remote sensing image data contains geometric and radiometric distortions.[26] Geometric distortions are errors in the position of a pixel relative to other pixels in the scene. They can result from the sensors' characteristics, the uncontrolled remote sensing platform's position, velocity, and altitude, and the earth´s curvature and rotation. On the other hand, radiometric distortions are differences in the measured brightness values in pixels in objects or from band to band. They can result from sensor errors, the wavelength dependence of solar radiation, and atmospheric conditions. [22]

Remote-sensing imagery requires radiometric calibration before analyzing data. Without a calibration process, researchers cannot compare and contrast data captured over different days or at different times. There are several radiometric calibration levels. As shown in Figure 5, radiometric calibration converts an image's raw digital pixel values to spectral radiance, then to surface reflectance values.

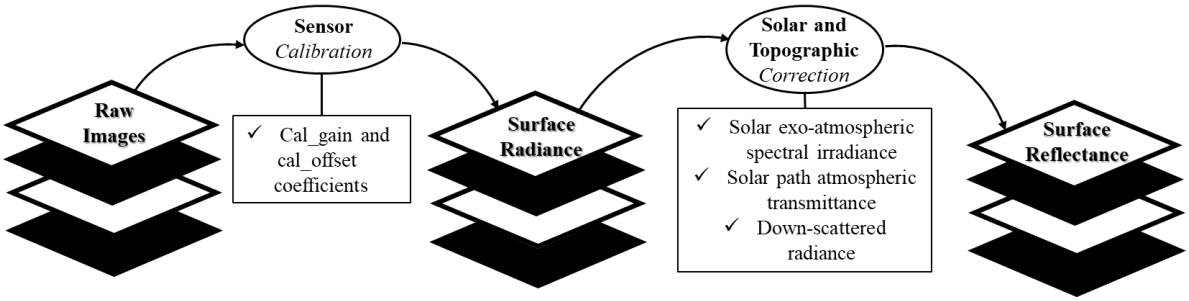

Figure 5 Data flow for calibration of remote sensing images

The first level converts values of digital numbers (from raw imagery) to spectral radiance. Since it requires sensor calibration information, it is known as sensor calibration or calibration-to-radiance. The standard calibration coefficients are gain and offset. Gain refers to the slope of the detector curve. On the other side, offset results from residual electronic noise present in the detector at any temperature other than absolute zero, even when there is no radiation.[22] At this level, radiometric calibration can include compensation for dark pixel offset and optical chain vignette effects.

The second level converts spectral radiance to reflectance, known as scene calibration or "calibration-to-reflectance." Reflectance refers to the amount of light reflected and absorbed by an object. This level requires information about atmospheric and lighting conditions and surface terrain at the time and location of capturing the images. When an atmosphere is present, two effects distort imagery. They are the absorption and scattering by the particles in the atmosphere. While absorption is a selective process that converts incoming energy into heat, radiation scattering depends on wavelength and particle size. [22] Moreover, variations in altitude and attitude of a remote sensing platform lead to a scale change at constant IFOV and image rotation. [22]

3.5 Spectral Signature

A spectral signature, also known as spectral response, refers to the amount of light reflected as a function of wavelength by an object.[25] The reflection characteristics of an ideal reflector would be a constant at 100% reflectance over the range. However, every surface and object reflects and absorbs the sun's radiation differently. In an image, brighter pixels mean objects reflect more light, whereas darker pixels mean objects absorb light.

Different objects tend to have different spectral responses in various bands. The selective absorption characteristics are associated with physical and biochemical composition. [27] Differences in spectral signatures are essential to identifying and segmenting surfaces and objects within each spectral band. [25] Figure 6 shows how three broad surface cover types of bare soil, vegetation, and water reflect light over the wavelengths between 400 and 2600 nm. The illustration is from the book *Multispectral Image Analysis Using the Object-Oriented Paradigm*.[2]

Clear water reflects less than 10 % in the blue and green channels, a smaller percentage in the red channel, and no energy in the infrared range. In the case of water containing suspended sediments, there is an increase in reflected light in the near-infrared region. The same applies to shallow water that allows reflection from the bottom material.

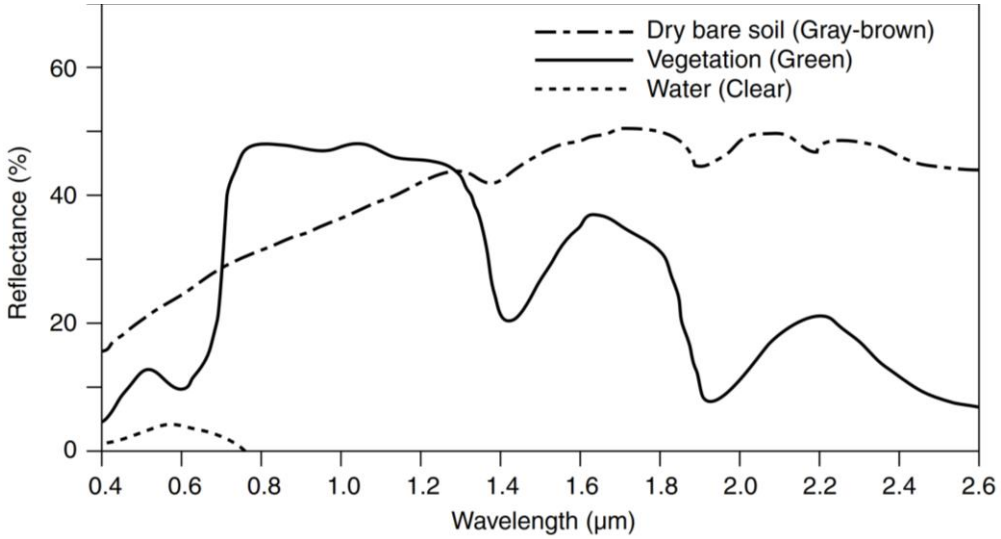

Figure 6 Spectral Signatures of water, dry soil, and green vegetation

Soils have a reflectance that increases approximately at the same rate from 400 and 1200 nm; nonetheless, the spectral response differs afterward depending on water content. Moisturized soil shows noticeable dips centered at 1400, 1900, and 2700 nm, caused by liquid water absorption. Dry soil and sand present unnoticeable dips at 1400 and 1900 nm. At above 2000 nm, their reflectance decreases slowly as wavelength increases.

Vegetations´ light reflectance is more complex and variable than soil or water. Its light reflectance depends heavily on growth state, stress levels, plant vigor, and moisture content. [15] Green and healthy vegetation, as shown in Figure 6, has a diverse spectral response. Water absorption bands (near 1400, 1900, and 2700 nm) dominate with downward trends in the middle infrared range. Plant cell structure influences the reflected light from 700 nm to 1300 nm. The reflectance of healthy vegetation is much stronger than the soil´s reflectance in the red-edge (717 nm) and near-infrared (842 nm) channels. Hence, differences in the reflected light in the NIR band are essential to map vegetation on the ground. Moreover, photosynthetic pigmentation is critical for low reflectance in visible wavelengths. Chlorophyll absorbs light in the blue (475 nm) and red (668 nm) bands for photosynthesis while leaving only a green reflection (560 nm).[28] Thus, chlorophyll

pigmented plants are visible as green, and Figure 6 displays a reflectance of less than 10% in blue and red bands. If the plant matter has different pigmentation, then the shape of the curve in the visible wavelength range will be different.

Solar energy interacts with healthy and stressed vegetation across the visible and non-visible spectrum to produce its optical properties. Since biochemical and biophysical characteristics determine vegetation absorption and reflectance properties. [3] Therefore, healthy and stressed plants have different spectral signatures.

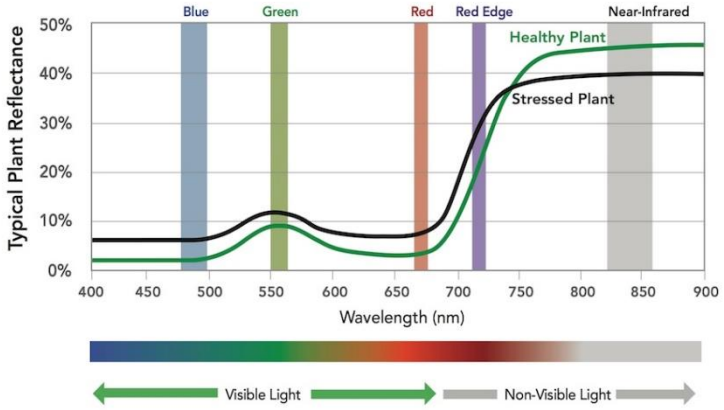

Figure 7 Spectral Signature of Healthy and Stressed Plants

Reflectance patterns in the visible spectrum are primarily due to photosynthetic pigments that absorb about 90% or more of the incoming radiation. The mainly photosynthetic pigments are chlorophylls and carotenoids. However, stressed vegetation presents a loss of photosynthetic chlorophyll, so the absorption dips in the blue and red bands fill up.[25] As a result, leaves appear yellowish and brownish. Beyond the visible red bands, the pattern abruptly reverses, as shown in Figure 7. This region of rapid change in reflectance is called the red-edge band. High reflectance is characteristic of the NIR band because there are no strongly absorbing molecules. [28] Nonetheless, stressed plants absorb more energy than healthy plants on the NIR bands.

3.6 Vegetation Indices

Vegetation Indices (VI) are algebraic combinations of different spectral bands; constructed from reflectance measurements. They exploit the unique spectral signature of vegetation on different bands while minimizing the response of various background

materials. Background materials, around and under vegetation, include soil and body waters.

Differences between spectral signatures relate to differences in biochemical composition and concentration of pigments, water, and cell wall structural materials. Therefore, researchers design each vegetation index to highlight specific plant properties in images, such as leaf area, canopy biomass, absorbed radiation, water stress, and chlorophyll content. [24] Variability in VIs can arise from atmospheric effects, viewing, and illumination angles, so radiometric calibration is critical. Regardless of variability, vegetation indices help monitor health conditions, map soil properties, calculate biomass, and segment plants and fruits from the background. [29]

3.6.1 Simple Ratio or Ratio Vegetation Index (RVI)

The Ratio Vegetation Index (RVI) captures the contrast between the red and infrared bands for vegetable pixels. It is also known as Simple Ratio (RS). Since the RVI is a ratio, the calculations reduce noise from variable illumination. Nonetheless, the Simple Ratio is susceptible to division by zero errors. [30] The equation for RVI is:

$$SR\ or\ RVI = \frac{NIR}{RED}$$

SR values for bare soil generally are near 1. As the biomass or canopy cover increases, so do the SR values. It is susceptible to vegetation and has a good correlation with plant biomass.

3.6.2 Normalized Difference Vegetation Index (NDVI)

The Normalized Difference Vegetation Index (NDVI) is the difference between the near-infrared and red bands, normalized by the sum of those bands. The normalization aims to balance out the effects of uneven illumination, such as shadows of clouds or hills. [31] The equation of NDVI is:

$$NDVI = \frac{NIR - RED}{NIR + RED}$$

The value of the NDVI ranges from -1 to +1. While close to zero values mean no vegetation, negative values indicate non-vegetated surfaces such as water, barren areas, ice, snow, or clouds. [30] Vegetated areas yield positive NDVI values due to high NIR and low red

reflectance. NDVI results close to a positive one (0.8 to 0.9) indicate the highest possible density of healthy green leaves. In contrast, NDVI values close to 0.2 and 0.3 represent unhealthy or sparse vegetation. Hence, the NDVI is commonly used for drought assessment, monitoring seasonal variation in vegetative vigor. Researchers also use it to segment vegetated from non-vegetated areas and estimate crop yield and biomass. [32]

3.6.3 Normalized Difference Red Edge (NDRE)

The Normalized Difference Red Edge (NDRE) is the difference between the near-infrared and red-edge bands, normalized by the sum of those bands. Since red-edge light penetrates a leaf more deeply than blue and red wavelengths, it is sensitive to the medium and high chlorophyll content and leaf nitrogen. [33] The equation of NDRE is:

$$NDRE = \frac{NIR - REDGE}{NIR + REDGE}$$

The value of the NDRE ranges from -1 to +1. High values of NDRE represent higher levels of leaf chlorophyll content. Soil typically has the lowest values, whereas unhealthy plants have intermediate values. The uses of NDRE include monitoring plant vigor in mid to late seasons and detecting fertilizer demand (especially nitrogen).

3.6.4 Chlorophyll Index (CI)

The Chlorophyll Indexes (Cl) are responsive to chlorophyll content in leaves. The Green Chlorophyll Index (CIg) uses the reflectance ratio between the NIR and green bands. In contrast, the Red Edge Chlorophyll Index (Clr) uses the reflectance ratio between the NIR and red-edge channels. The equations of the CIs are:

$$CIg = \frac{NIR}{GREEN} - 1$$

$$CIr = \frac{NIR}{REDGE} - 1$$

The CIg and CIr values are sensitive to slight variations in the chlorophyll content and consistent across most species. Since chlorophyll content directly depends on nitrogen level in plants, both CIs help detect areas with yellow or shed foliage. Additional applications include estimating the leaf area index (LAI).[34]

3.6.5 Normalize Difference Water Index (NDWI)

The Normalized Difference Water Index (NDWI) is susceptible to variations in hydrological conditions. It delineates open water bodies and assesses their turbidity, mitigating the reflectance of soil and land vegetation cover.[35] It is also helpful for monitoring leaves water content and displaying plant water stress. The index takes advantage that water bodies have low reflectance in green and near-infrared bands. The equation of NDWI is:

$$NDWI = \frac{GREEN - NIR}{GREEN + NIR}$$

The value of the NDWI ranges from -1 to +1. NDWI values above 0 represent water bodies, whereas NDWI values indicate the absence of water bodies. Nevertheless, water bodies can also have NDWI values less than 0 due to bare sediment in some rivers, lakes, and seas. [36]

3.6.6 Visible Atmospherically Resistant Index (VARI)

The Visible Atmospherically Resistant Index (VARI) detects vegetation while mitigating illumination and atmospheric effects. It is ideal for color images because it uses bands of the visible electromagnetic spectrum. The following equation defines VARI:

$$VARI = \frac{GREEN - RED}{GREEN + RED - BLUE}$$

The value of the VARI ranges from -1 to +1. VARI is less sensitive than NDVI to atmospheric effects because it needs to subtract the blue channel in the denominator. [37] It is ideal for crop state assessment when minimum sensitivity to atmospheric effects is required.

4. Methodology

Throughout the study, the datasets contained remote-sensed multispectral images from several crops, including blueberry, maguey, and pineapple. Each dataset corresponded to a particular experiment on a crop, and they had different environmental conditions. The following were the three datasets:

1. Inoculated Blueberry with Ericoid Mycorrhizal (ErM) Fungi.
2. Infected Agave with Cercospora Agavicola
3. Pineapple Plantation

Precision Agrícula, private company, lent the MicaSense multispectral cameras to take the images: RedEdge-MX and RedEdge-P. The lead researcher took the captures from the dataset of 'Inoculated Blueberry with Ericoid Mycorrhizal (ErM) Fungi' and 'Infected Agave with Cercospora Agavicola' with the RedEdge-MX. On the other hand, an expert from Precision Agricola used the RedEdge-P multispectral camera to capture the 'Pineapple Plantation' dataset. Table 4 compares the basic specifications of MicaSense RedEdge-MX and RedEdge-P. For specific details of a dataset's image acquisition process, refer to each dataset's section.

Specification	RedEdge-MX	RedEdge-P
Spectral resolution	5	6
Spectral bands Multispectral (MS) Panchromatic (PAN)	Blue (475 nm) Green (560 nm) Red (668 nm) Red-Edge (717 nm) Near-Infrared (842 nm)	Blue (475 nm) Green (560 nm) Red (668 nm) Red-Edge (717 nm) Near-Infrared (842 nm) Panchromatic (634.5 nm)
Resolution per sensor	1280 x 960 px	1456 x 1088 px (MS bands) 2464 x 2056 px (PAN)
Output bit depth	12-bit	12-bit
Ground Sample Distance at 120m (~400ft)	8.2 cm/px	7.7 cm/px (MS bands) 3.98 cm/px (PAN)
Capture rate (all bands)	One capture per second	Three captures per second
Field of View	47.2° HFOV	50° x 38 (MS bands) 44° x 38° (PAN)

Table 4 Basic Specifications of MicaSense RedEdge-MX and RedEdge-P

The multispectral cameras stored files in the storage device in a folder structure. Each time the camera was powered up, it created a new folder, for example, '0000SET' and

‘0001SET’. Within each folder, the camera created a subfolder with the images starting from ‘000’. If more than 200 images were stored, the camera created a second folder named ‘001’, and so on. Each subfolder stored groups of TIFF files for each image capture. The suffix at the end of each file indicated the band name, center wavelength, and bandwidth, as shown in Table 5. Depending on the setting, the TIFF files are 12-bit resolution and stored in either 12-bit or 16-bit TIFF RAW format. Metadata tags are embedded for each file in standard EXIF format.

Band Number	Band Name	Center Wavelength	Bandwidth (nm) RedEdge-MX	Bandwidth (nm) RedEdge-P
1	Blue	475	20	32
2	Green	560	20	27
3	Red	668	10	16
4	Near Infrared	840	40	12
5	Red Edge	717	10	57
6	Panchromatic	634.5	Not Applicable	463

Table 5 Spectral Bands of RedEdge-MX and RedEdge-P

4.1 Processing Workflow

For RedEdge or Altum imagery, MicaSense partners provide plug-and-play software for processing and analysis, including Pix4D, Agisoft Photoscan, ENVI, and Solvi. The study implemented an image processing workflow using the MicaSense Image Processing repository. The repository contains tutorials, examples, and libraries for processing RedEdge and Altum images using Python, OpenCV, Matplot, and more. The intention was to control the entire radiometric workflow and implement a methodology for processing imagery using open-source tools.

Multispectral cameras measured each band's radiation and converted the radiance into raw images. Raw images are composed of pixels containing a digital number (DN) describing the radiation intensity through a range of brightness values. Figure 8 shows the raw images of blueberry crop 0001 from the Blueberry dataset with the vintage color map. The colorbars on the right represent the mapping of digital numbers to colors in each channel. The images required 0 to 65536 digital numbers because the camera stored the bands in 16-bit TIFF files. In alignment with crop spectral response, the NIR and RedEdge images measured higher radiation than the RGB spectrum.

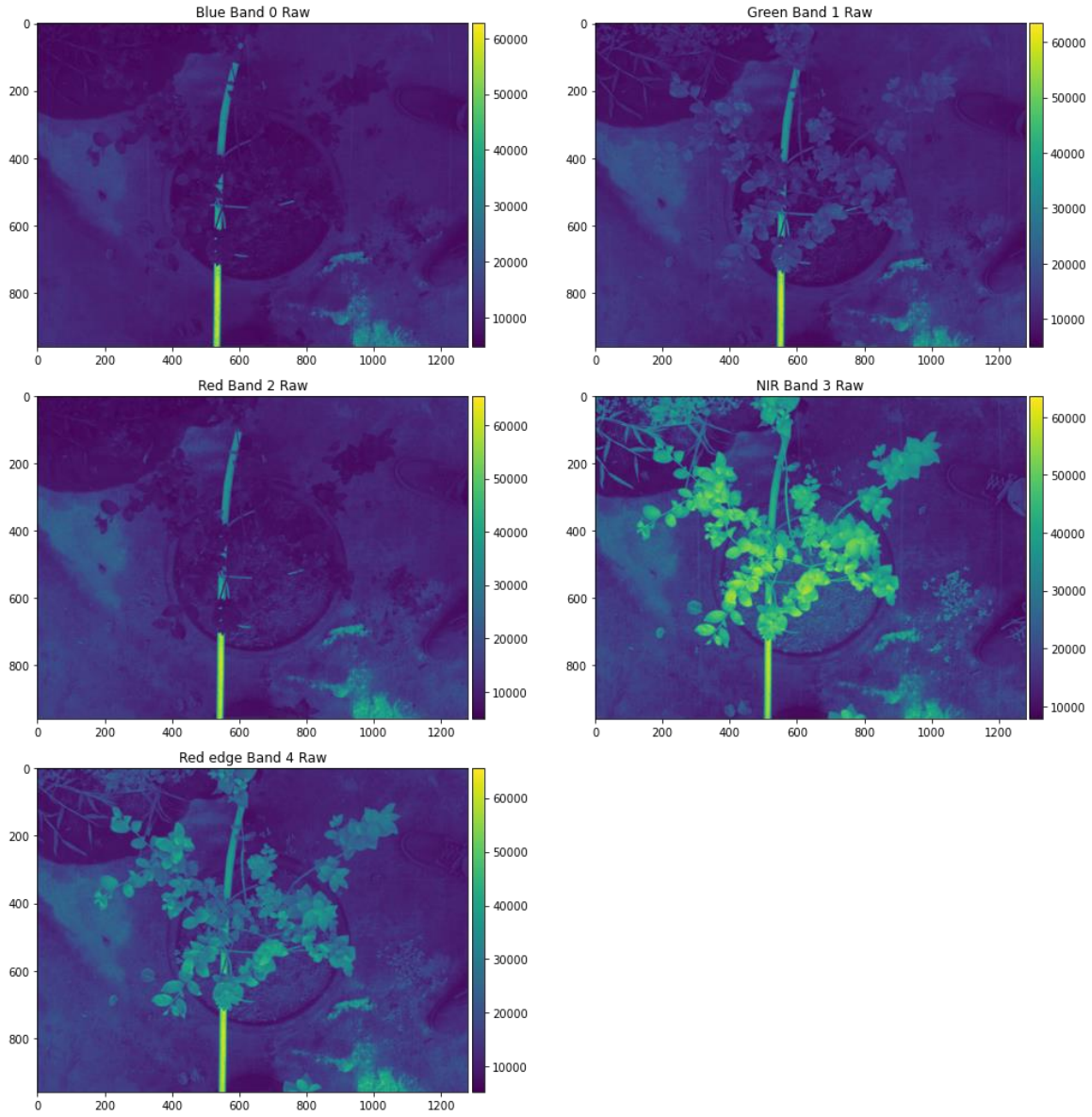

Figure 8 Blueberry 0001 Raw Images

Since pixel's DN values were relative to captured lighting conditions, radiometric calibration was necessary. The radiometric workflow enabled comparing and contrasting reflectance data over flights, dates, and weather conditions. According to Micasense, their custom radiometric calibration model has two levels, as shown in Figure 5: sensor´s calibration and calibration-to-reflectance.

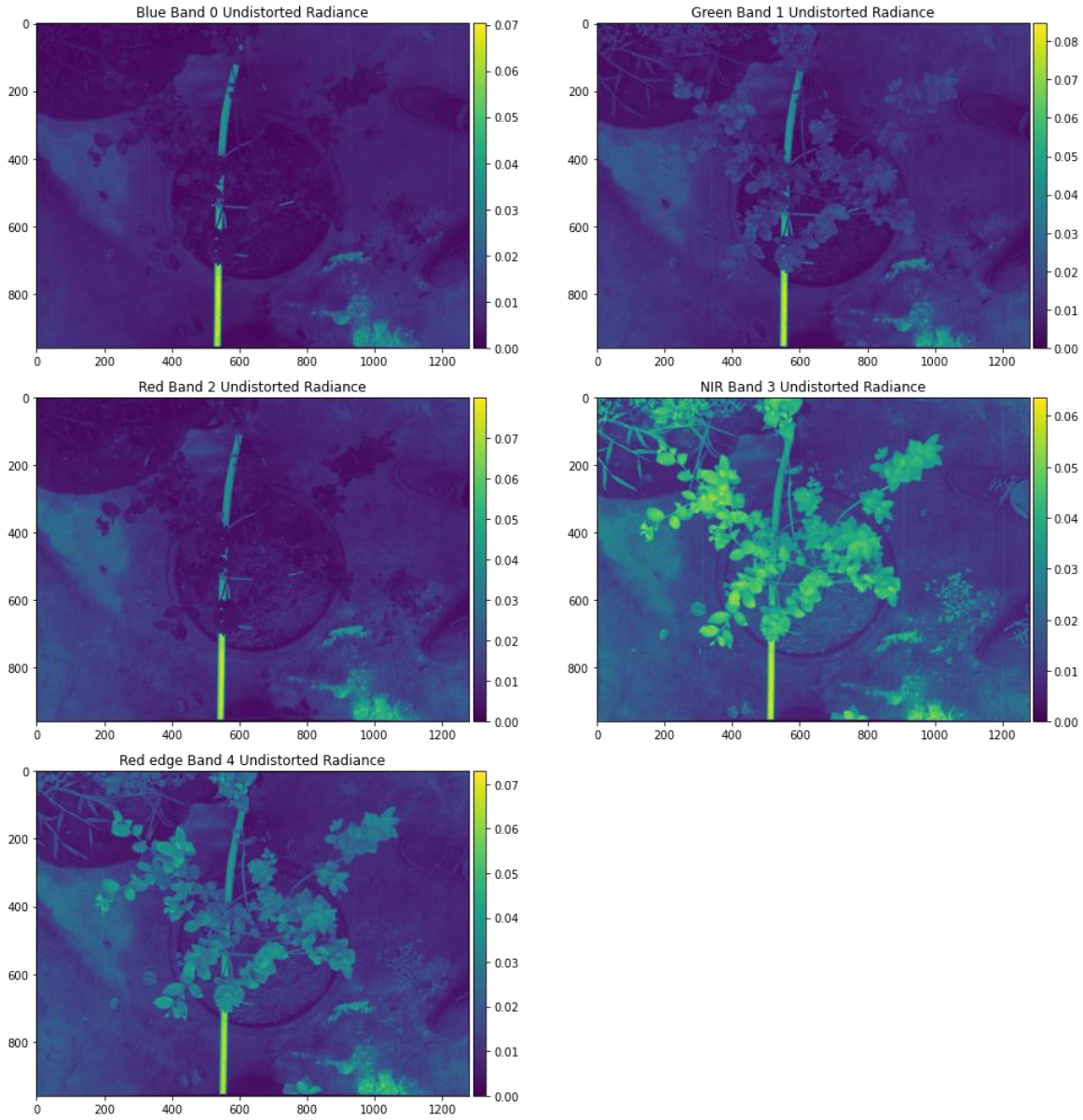

Figure 9 Blueberry 0001 Radiance Images

The first level converted raw digital numbers to spectral radiance values, with W/m2/sr/nm units. The sensor´s calibration level compensated for dark pixel offset, electro-optical effects of sensors, lens vignette effects, and incident light at the time of capture. It also removed the lens distortion. Correcting the lens distortion ensured that straight lines in the images were straight. The parameters required for the sensor´s calibration were in the metadata inside each image. Exiftool, an open-source tool package, allowed reading image metadata. According to MicaSense´s documentation, the formula for computing the spectral radiance L from pixel value p is:

$$L = V(x,y) * \frac{a_1}{g} * \frac{p - p_{BL}}{t_e + a_2 - a_3 * t_e * y}$$

Table 6 defines and describes each symbol for computing the spectral radiance L from pixel value p. Figure 9 displays the undistorted radiance images of blueberry crop 0001 from the Blueberry dataset with the vintage color map. The radiance images have values from 0 to 0.09 W/m2/sr/nm, as shown in the colorbars.

Symbol	Name	Description
p	Normalized raw pixel value	$p = \frac{DN\ for\ the\ pixel}{radiometric\ resolution} = \frac{DN_{(x,y)}}{2^m}$ Where m was the number of bits in the images.
p_{BL}	Normalized black level offset	It corrected the small random charge generation in each pixel, independent of incoming light.
a_1, a_2, a_3	Radiometric calibration coefficients.	It compensated for imager-specific effects due to inaccuracies of the CMOS imager pixels.
$V(x,y)$	Vignette polynomial function	It corrected the fall-off in light sensitivity that occurs in pixels further from the center of the image, known as dark corners.
t_e	Image exposure time	The camera adjusted the exposure time to prevent pixel saturation.
g	Sensor gain setting	Gain is based on the photographic parameter ISO of 100.
x,y	Pixel location	X is the column number, and Y is the row number inside an image.

Table 6 Spectral Radiance L

The second level converted calibrated spectral radiance into reflectance, which refers to an object's amount of light reflected and absorbed. For the “calibration-to-reflectance” level, collecting solar irradiance data for each flight was critical. MicaSense provides a Calibrated Reflectance Panel (CPR), a gray plastic box containing an albedo panel (white square), a QR code, and certified reflectance data.

Images of the calibrated panel pre- and post-flight accurately represented the amount of light reaching the ground at the date, time, and location. The albedo panel is a unique material that reflects incident light equally in all directions. Hence, the calibrated panel images helped determine the transfer function of radiance to reflectance for each band.

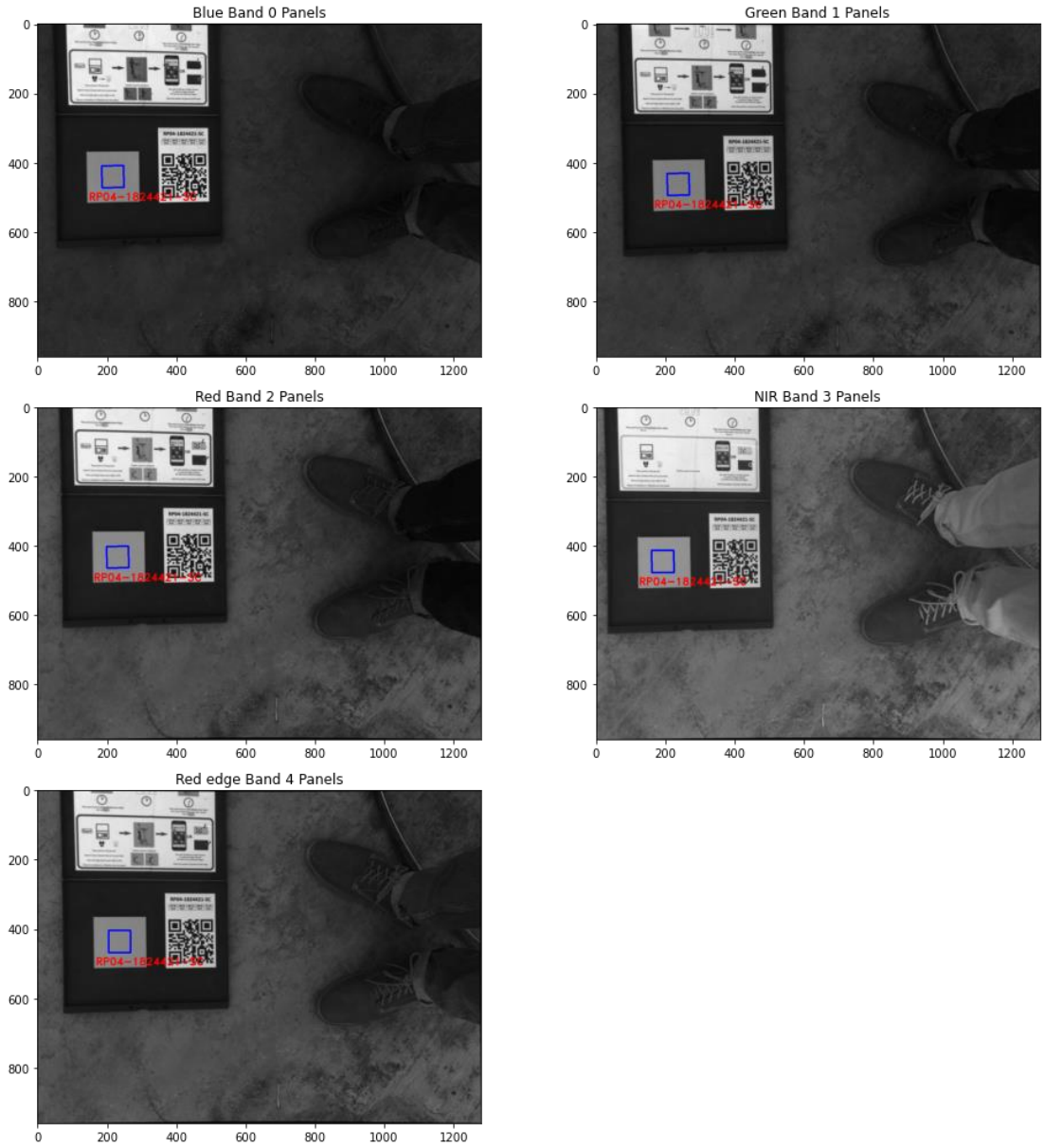

Figure 10 Calibrated Reflectance Panels (CRP)

Before calculating the transfer functions, panel images went through the sensor´s calibration level. Then, the code extracted the average radiance for the pixels inside the albedo panel, as shown in Figure 10. The code displays a blue square per channel, representing the smaller region used to extract the radiance of the albedo. The QR code helped locate the albedo panel's position automatically. Since MicaSense provides the panel reflectance values of each channel, we calculated the transfer function using the formula:

$$F_i = \frac{p_i}{avg(L_i)}$$

Where F_i is the reflectance calibration factor for the ith band, p_i is the average reflectance of the calibrated reflectance panel, and $avg(L_i)$ is the average radiance value for the pixels inside the panel for the ith band.

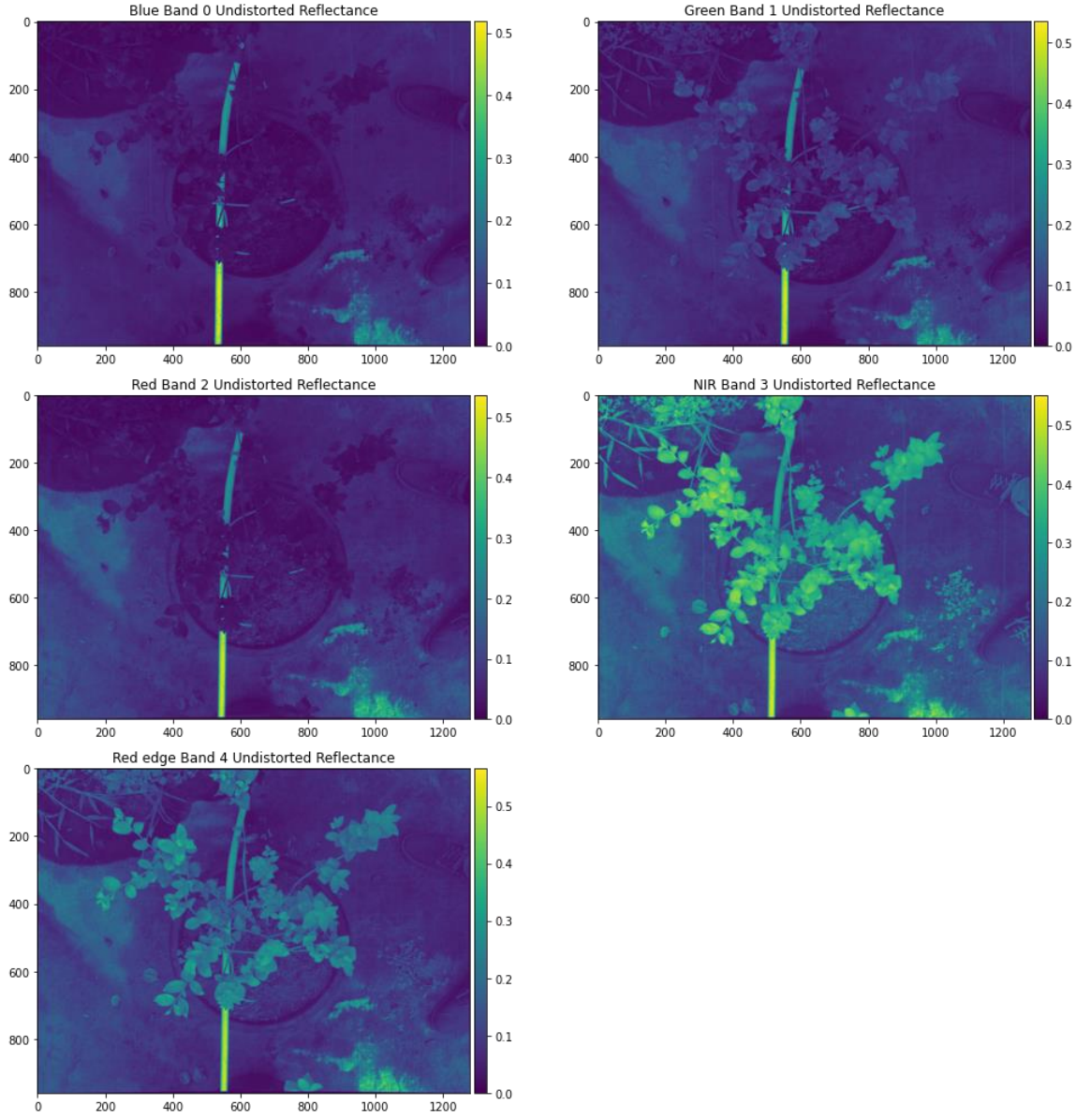

Figure 11 Blueberry 0001 Reflectance Images

The transfer function was used for the ith band to scale radiance into reflectance images by multiplying the radiance values of any image by the factor F_i. This method is the standard scientific calibration method of surface reflectance. Since it is straightforward, repeatable, and sufficient for this study, the Downwelling Light Sensor (DLS) was not incorporated into

the calibration process. The DLS measures the spectral irradiance from the sky for the camera's spectral bands. So, its data helps to account for changing irradiance over time.

The output of the radiometric calibration is a reflectance image for each band. Figure 11 shows the reflectance images of blueberry crop 0001 from the Blueberry dataset with the vintage color map. The reflectance images have values from 0 to 0.6 (or 60%). Reflectance higher than 1.0 (or 100%) occurs when objects in images reflect most incident light in one direction. Examples include the reflectance of the sun on a car's surface or an extensive body of water.

The next step was band-to-band alignment, also called image alignment. Since RedEdge cameras have an independent lens for each band, the camera captured the images from slightly different viewing angles. MicaSense specifies that its cameras do not align the five bands mechanically. As a result, the location of objects in one channel is different from the others.

Image alignment involves the techniques for manipulating an image so that objects (features) in the two lines up. A warp matrix relates two images with different views of the same scene. Image alignment algorithms estimated the warp matrix based on motion models such as translation, Euclidean, affine, and homography. The transformation matrix, as it is also known, contained the parameters to shift from the first to the second view. In other words, multiplying the warp matrix with the points in the first view made it possible to find the corresponding locations in the second.

The MicaSense repository and custom code helped with the image alignment. The code found a transformation matrix to align each band to a reference band, using the lens in the middle as a reference. The lens in the middle corresponded to the Red Edge band, image number four. After the band-to-band alignment, algorithms removed pixels around the edges which did not overlap in all bands. Also, the code cropped pixels at the edges, as shown in Figure 12. Suitable transformation matrices are stable over a planned flight unless the camera undergoes a shock event.

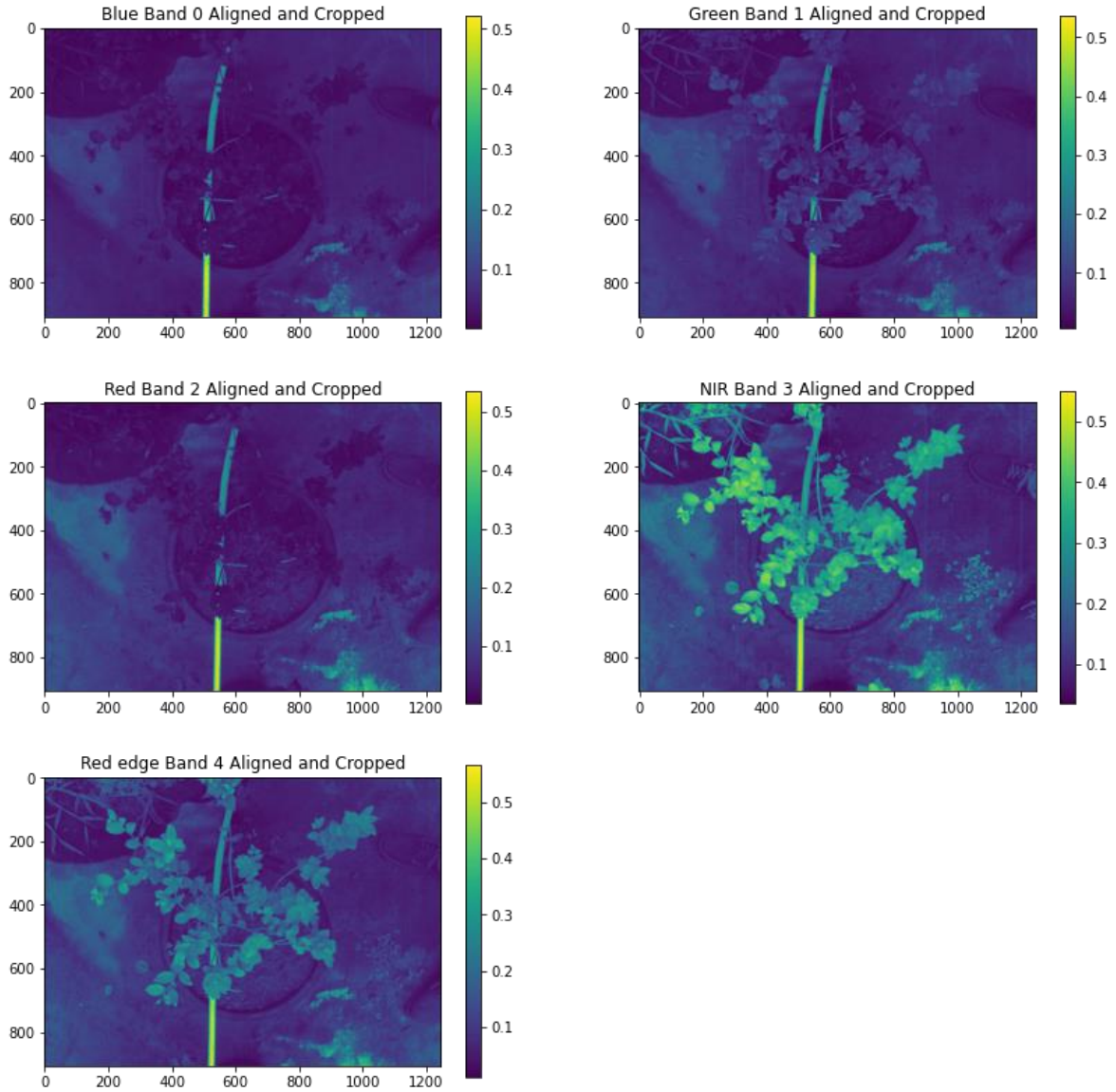

Figure 12 Blueberry 0001 Aligned Images without cropping

Image alignment allowed the combinations of bands into true-color (RGB) and false color (CIR) composites. They were helpful for scouting and visualizing using single images. In addition, image alignment helped to compute vegetation indices to analyze images. The computed vegetation indices were the NDVI, NDRE, CIg, Cir, and simple ratio. Also, the code computed the histogram, which was used to pick colormap ranges for improving visualization.

4.2 Dataset: Inoculated Blueberry with Ericoid Mycorrhizal (ErM) Fungi.

Mexico has become an emerging power in the blueberry market in the last ten years, as shown in

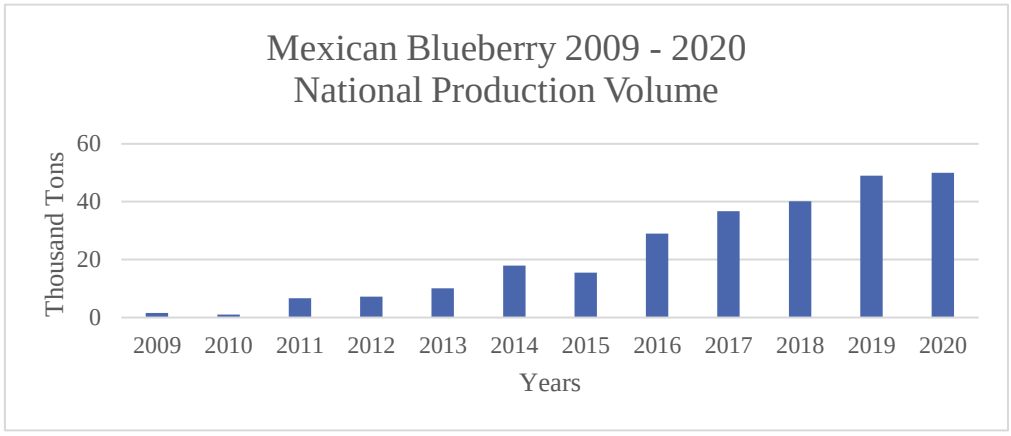

Figure 13. According to the 2021 Food and Agricultural Overview of SIAP, Mexico was the 6th world producer, with 50,293 tons in 2020. [38] Moreover, the blueberry exports represented the total trade flow of 398.6 million. The crop is a deciduous shrub of 20 to 60 cm in height. Its fruits are light-blue spherical berries measuring 1 to 3cm in diameter. The factors driving the production and commercialization of blueberries in Mexico include the rapid return of the investment (ROI), high profitability, good versatility for its fruit consumption, and high export potential. [39]

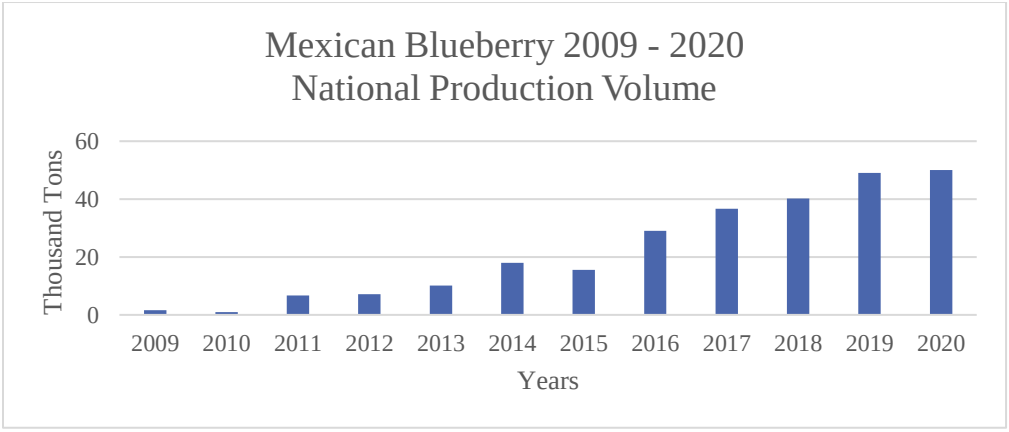

Figure 13 Mexican Blueberry 2009-2020 National Production Volume, retrieved from the Food and Agriculture Organization of the United Nations

Several studies showed the benefits of the symbiosis between blueberry plants and ericoid mycorrhizal fungi. *Ericoid Mycorrhizal* (ErM) fungi enhance Ericaceous plants' growth. The

ErM fungi increase access to water and nutrients in exchange for aboveground photosynthate. [40] Moreover, the addition of organic fertilizers to inoculated cultivated blueberries increased nutrient uptake and nutrient use efficiency in several cultivars.[41] Another study demonstrated that inoculating highbush blueberries with ErM fungi enhanced flowering and significantly altered floral traits and reproduction in several cultivars. [42]

The dataset corresponded to an experiment that took place in a greenhouse at *Centro Universitatio de Ciencias Biologicas y Agropecuarias* (CUCBA) of the University of Guadalajara, Jalisco, Mexico. The experimental area had a topological arrangement of 2.2 m between rows and 0.6 m between pots. The study aimed to compare ErM fungi and fertilizer's potential role in fruit production and plant development in two blueberry variants (Biloxi and Sharp blue). The researcher inoculated with commercial ErM fungus *Oidiodendron sp.* and *Rhizoscyphus Ericae* and manually measured temperature, soil ph, and leaves features.

The experiment started in September 2020 and was supposedly going to produce fruits three times per year. Unfortunately, four factors led to the experiment's termination in November 2020. First, the COVID19 pandemic made it challenging to access the greenhouse, nurture the crops, and capture images. Second, federal budget cuts in public funding shrank the number of projects running at the University of Guadalajara. Third, the principal researcher dropped his master´s degree in agriculture due to financial problems. Finally, outsiders from the experiments pruned the blueberry trees incorrectly and contaminated the plantation with a disease. By November, the experiment area had been cleaned and sanitized.

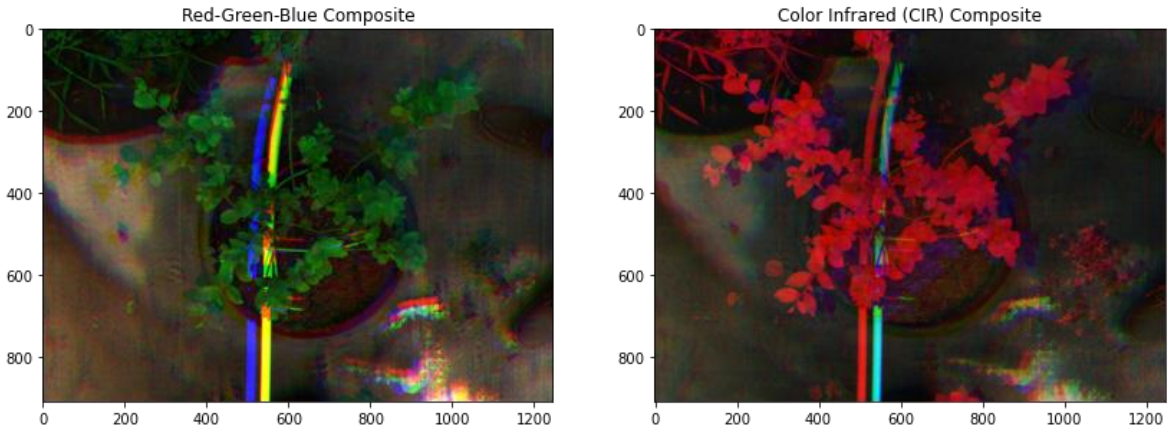

Figure 14 Blueberry RGB and CIR Composites

The dataset contained the captures of four 2020 dates: September 22, September 28, October 6, and October 12. Each capture contained five images corresponding to the spectral bands of blue, green, red, red-edge, and near-infrared. Before processing the captures, images were relabeled based on the date of capture. Duplicates were manually deleted from the dataset. Since images did not have an identification number, images were reorganized based on visual inspection. Without an image acquisition methodology, the captures contained several issues, problematic for image processing and analysis, as shown in Figure 14.

4.3 Dataset: Infected Tequila Agave with Cercospora Agavicola

Mexico leads in the production of tequila agave, with 1519 tons of tequila agave in 2020. [43] The tequila agave is a bushy plant distinguished by long and rigid sword-shaped leaves. A heart or pineapple is at the center, with the natural juice required for obtaining tequila. In the same year, the foreign trade of tequila was 2,355 million USD dollars. Thus, the factors driving the cultivation of tequila agave in Mexico include high profitability with tequila.

The dataset corresponds to an experiment in an open field at CUCBA of the University of Guadalajara, Jalisco, Mexico. The researcher bio-stimulated tequila agave through different treatments, such as bacteria, Trichoderma, seaweed, or a combination. The study aimed to monitor the propagation and resistance of plants against a disease called *Cercospora Agavicola*. The fungus's infection causes black oval lesions of up to 1-3 cm commonly found in the middle to the upper third of non-expanded leaves of the agave's head.[44] It develops rapidly, producing coalescing, depressed brown-grey spots. It ends with the head's collapse and the plant's death.

ID	Treatment	ID	Treatment	ID	Treatment
T1	Bacteria	T4	Bacteria	T7	Seaweed
T2	Trichoderma	T5	Seaweed	T8	Seaweed
T3	Bacteria and Trichoderma	T6	Silicon	T9	No Treatment

Table 7 Treatment ID and Description

The experiment started on September 6, 2019; agave plants had an average height of 12 cm, without roots. Table 7 shows the nine groups formed, five plants per group; eight received treatment while T9 was the control group. The researcher applied four doses at intervals of 15 days between doses. On March 4, 2020, the researcher inoculated the plants with the pathogen Cercospora Agavicola and captured the first images. The original intent of the multispectral images was to support the researcher's findings. Nonetheless, the lack of funding and collaboration between universities led to the termination of the association.

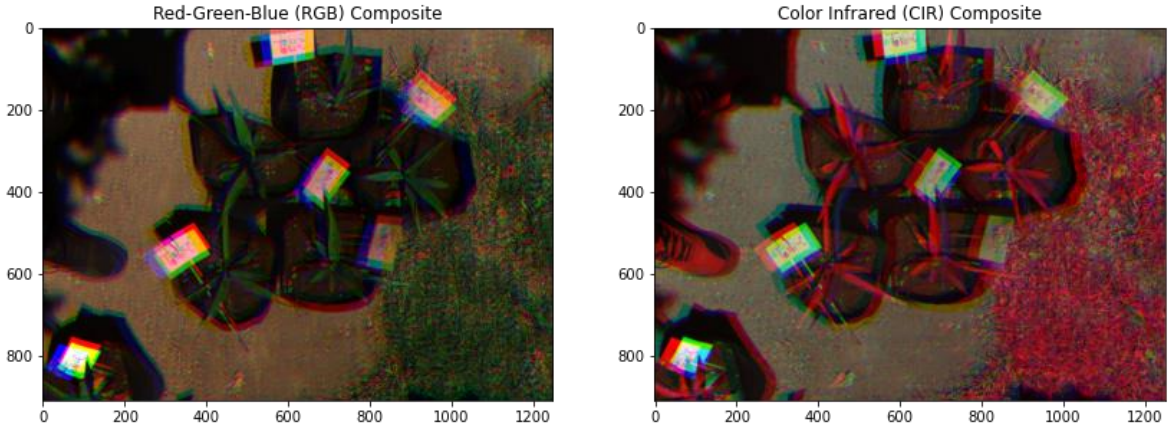

Figure 15 Tequila Agave RGB and CIR Composites

The dataset contained captures from March 4 to April 1, 2020. The researcher took images only for fifteen days in the morning and noon. After inspecting captures, the images in the morning seemed better taken. Figure 15 displays a sample of RGB and CIR composites after calibration. Without an image acquisition methodology, the captures contained several issues, problematic for image processing and analysis.

4.4 Dataset: Pineapple Plantation

Mexico stands as the ninth pineapple world producer, with a production of 1,200,000 tonnes in 2020. [45] In the same year, the foreign trade was 34.6 million USD dollars. The plant is a perennial herb that grows 1 to 1.5 m tall, with 70 to 80 leaves arranged in a spiral. The fruit is oval and thick, measuring 30 cm long and 15 cm in diameter on average.

The dataset corresponds to Precision Agricola's capture at the Dole pineapple plantation in San Carlos, Colombia. The crops were eight weeks, nine weeks, ten weeks, thirteen weeks,

fourteen weeks, and fifteen weeks old. Only the dataset of nine weeks old crops was shared. The main goal was fruit identification using vegetation indices. The experiment ended because Dole wanted to focus on banana plantations.

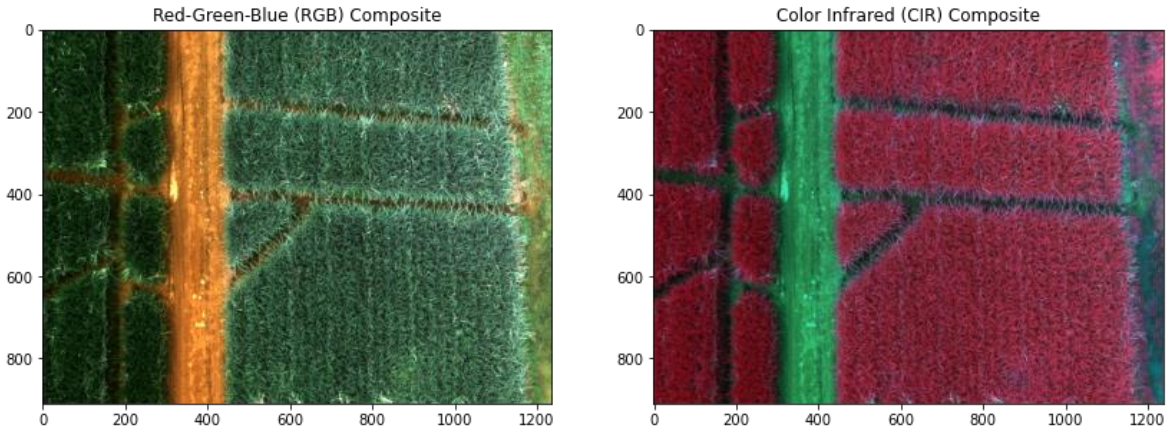

Figure 16 Pineapple RGB and CIR Composites

Each capture contained five multispectral images and one panchromatic image. In contrast with the other datasets, images required relabeling and reorganization. The subsample contained several images of the same subsection, taken from altitudes that range from 20 to 60 meters. Figure 16 shows the RGB and CIR composites of a sample of the pineapple plantation.

5. RESULTS AND DISCUSSION

5.1 Results

The dataset's captures from blueberry and tequila agave had several issues that generated high noisy composites and vegetation indices. Without a methodology for acquiring images, the reflectance images limited analysis.

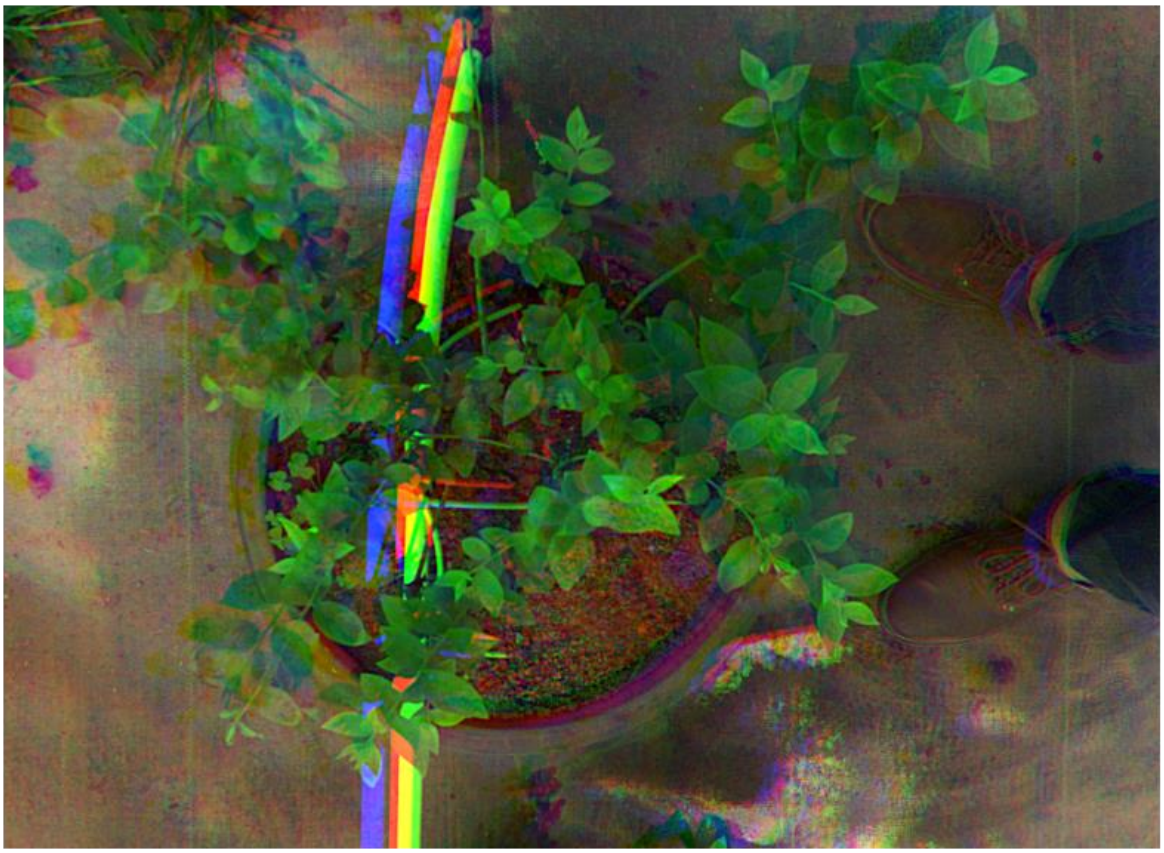

Figure 17 Blueberry 0002 enhanced RGB composite with alignment for high altitudes

Captures taken at low and high altitudes require different band-to-band alignment processes. Images captured from low altitudes generated unreliable results on the band-to-band alignment algorithm for high altitudes. At a 2-meter altitude, the composites and vegetation indices presented duplicates of leaves and branches, as shown in Figure 17. Duplicates were more apparent on leaves close to the upper and lower left sides than on the right. Aligning

bands considering the low altitude instead of the high significantly reduced the parallax errors, as displayed in Figure 18.

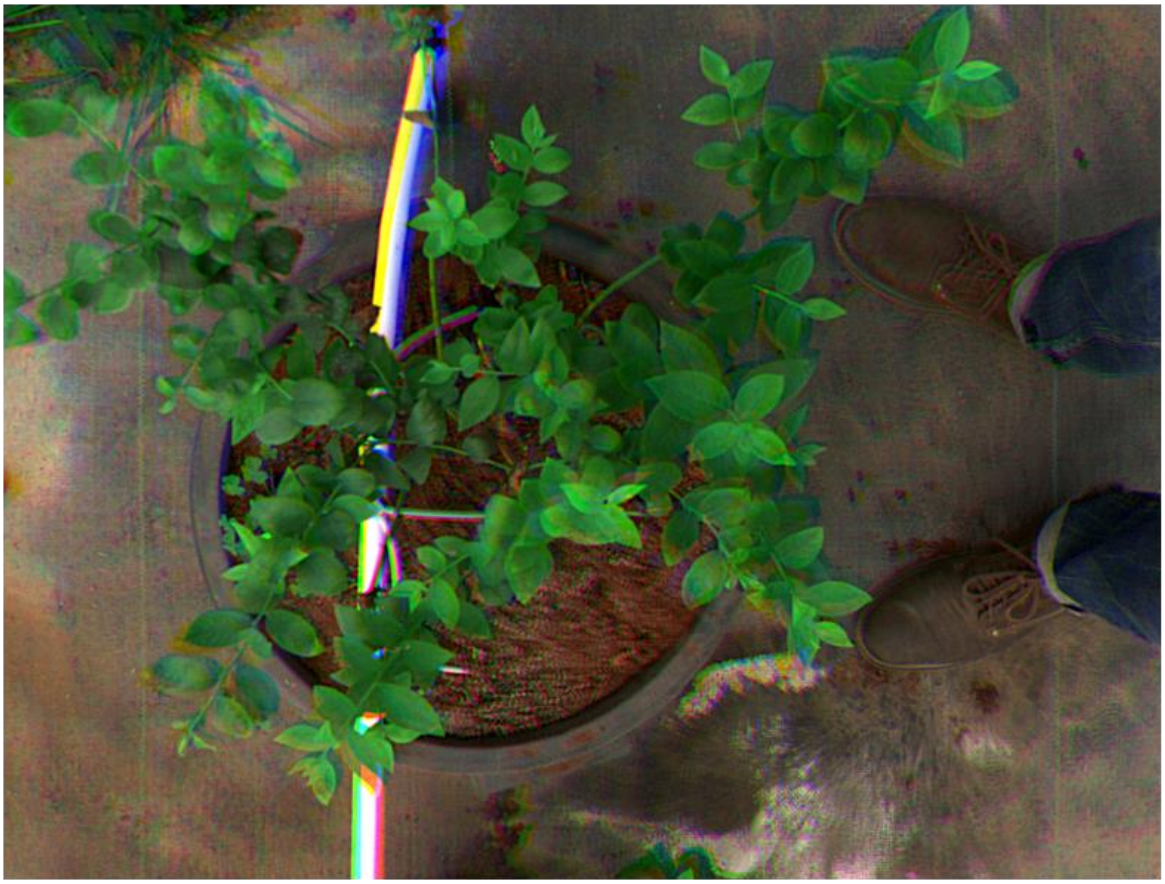

Figure 18 Blueberry 0002 enhanced RGB composite with alignment for low altitudes

White objects, such as tubes and papers, highlighted errors in the alignment of bands. On the RGB composite of blueberries, the white tube broke down into a green, a blue, and a red tube, as seen in Figure 17. With alignment for low altitudes, the tube presented fewer parallax errors; nonetheless, they were more visible at the tube ends, as shown in Figure 18. In the tequila agave dataset, the alignment errors were observable at the edges of the white papers used for labeling crops. In Figure 19, the paper's edges presented red, green, blue, or yellow colors.

Figure 19 Tequila Agave 0002 enhanced RGB composite with alignment for low altitudes

The blueberry and agave images contained objects unrelated to the study, generating significant noise in vegetation indices. Examples include grass, rocks, trash, shoes, and jeans, as displayed in Figure 19. After computing the vegetation indices, histograms of each vegetation indices helped identify crop pixels from the background. Then, the algorithm removed soil and shadowed areas based on reflectance values. Figure 22 shows the before and after masking the NVDI of sample 002 of tequila agave. The algorithm filtered out the white paper, soil, pot, wooden stick, and rocks.

Nevertheless, several pixels of shoes, jeans, and grass stayed. The blueberry NDVI, NDRE, Simple Ratio, and Red Edge Chlorophyll Index also presented the shoes and jeans on the right of the plant, as shown in Figure 20 and Figure 21. The masked NDVI displayed the plant´s vigor better than the masked NDRE because the blueberry was in an early development stage. The Simple Ration displayed that the plant segmented on pixels greater than 3.

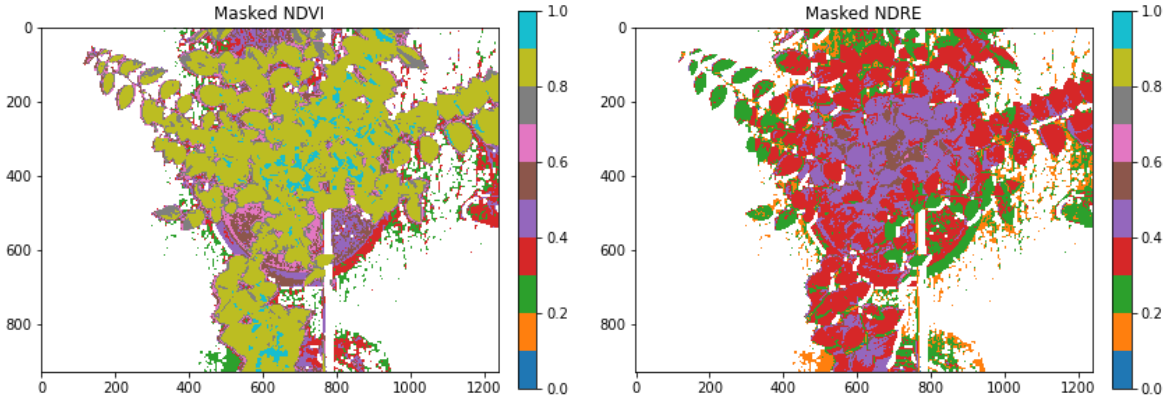

Figure 20 Blueber

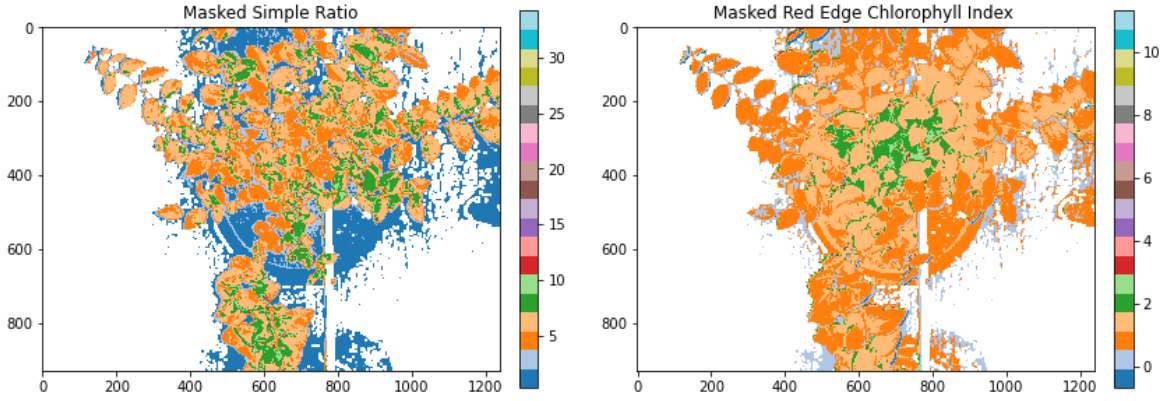

ry 003 Masked NDVI and Masked NDRE

Figure 21 Blueberry 003 Masked Simple Ratio and Masked Red Edge Chlorophyll Index

Image analysis based on vegetation indices presented a disadvantage. The vegetation indices and histograms were analyzed previously to understand and manually fine-tune the reflectance values for masking pixels. For instance, NDVI values lower than 0.1 were bare soil, while above 0.1 and below 0.5 are unhealthy plants, and healthy crops had NDVI values above 0.5. The algorithm filtered pixels of unwanted objects and pixels related to the biomass of crops, as shown in Figure 22. Since grass and agave had a similar spectral signature, it was impossible to neutralize the noise of grass without removing pixels from agave plants. Hence, further noise removal directly affected the number of pixels related to the plant's biomass.

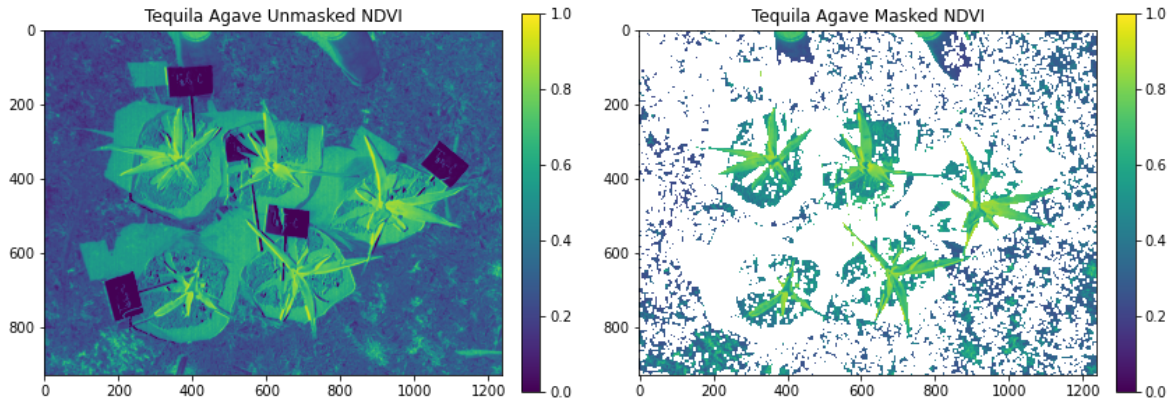

Figure 22 Tequila Agave 002 Unmasked and Masked NDVI

Vegetation indices exploited the spectral signature of crops on different bands to extract insights from multispectral data. Beforehand, a good understanding of the study´s goal and vegetation indices applications were a requirement.

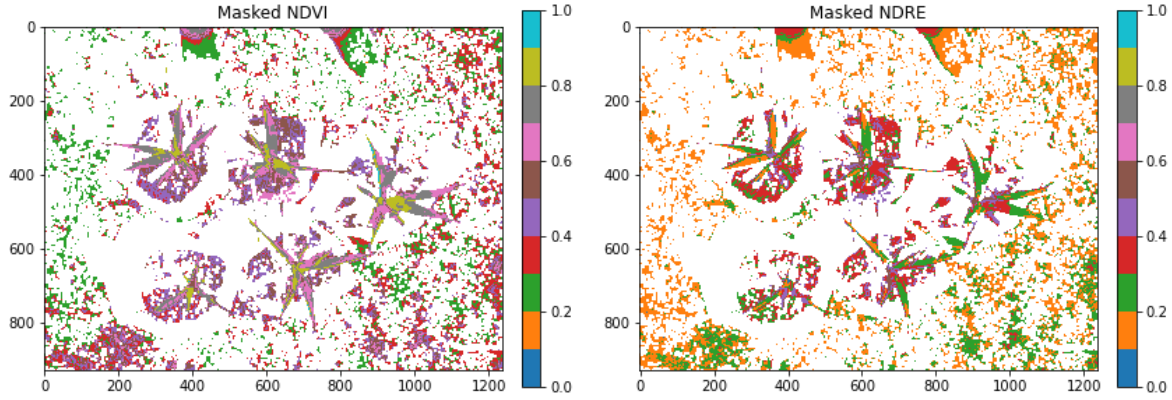

Figure 23 Tequila Agave 002 Masked NDVI and Masked NDRE

Literature and experimentation firstly suggested calculating the NDVI because of its effectiveness in distinguishing vegetation from the soil. After inspecting the NDVI histogram, the code replaced pixels with NIR reflectance of less than 20 percent to zero for removing non-plant and shadows. Then, the algorithm calculated the NDRE, the Red Edge Chlorophyll Index, and the Simple Ratio. Non-plant pixels were excluded and shown as transparent by masking areas with shadows and low NDVI pixels, which sometimes removed plant pixels. On the masked NDVI, the agave´s pixels had values between 0.6 and 0.9. The crops were identifiable regardless of the noisy images, as shown in Figure 23. Since the tequila agave plants were in an early stage and the NDRE is for mid/late-stage plants, the NDRE results were less meaningful than the NDVI. The plant´s pixels were between 0.1 and

0.3 in the NDRE, reflecting the minimum chlorophyll content in leaves. The Red-Edge Chlorophyll Index showed the same low chlorophyll content in Figure 24.

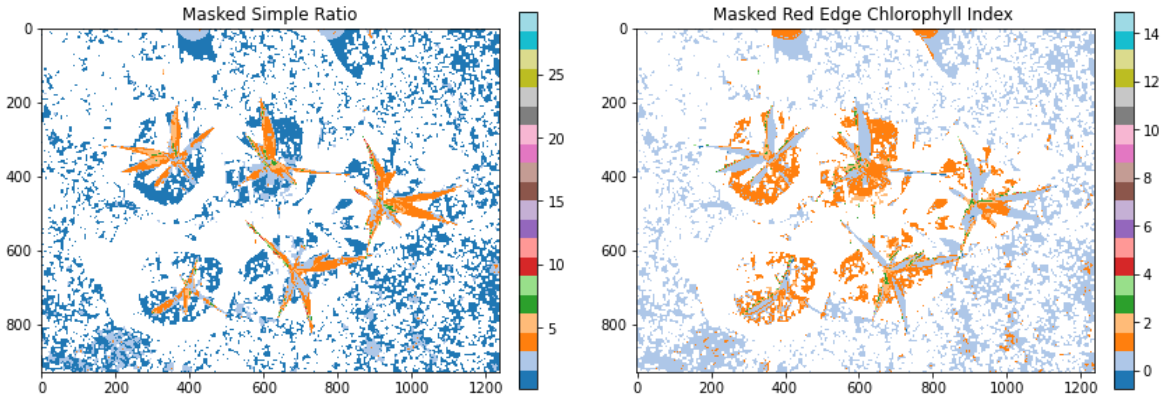

Figure 24 Tequila Agave 002 Masked Simple Ratio and Masked Red-Edge Chlorophyll Index

In the pineapple dataset, the aim was to identify fruits. The masked NDVI showed the segmentation of plants with values above 0.7, while the masked NDRE displayed plants between 0.6 and 0.8. However, the identification of fruits was unsuccessful in the NDVI, NDVI, Simple Ratio and Red Edge Chlorophyll Index, as shown in Figure 25 and Figure 26.

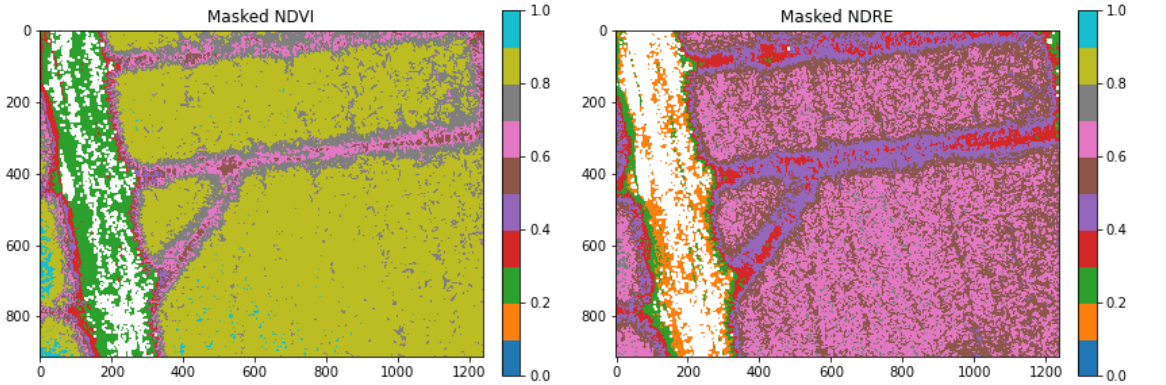

Figure 25 Pineapple 002 Masked NDVI and Masked NDRE

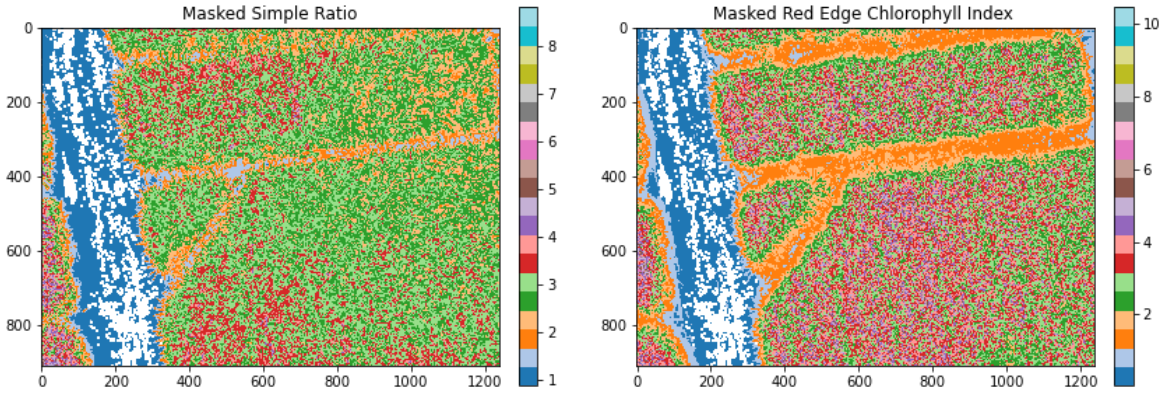

Figure 26 Pineapple 002 Masked Simple Ratio and Masked Red-Edge Chlorophyll Index

The other vegetation indices computed were the Green Chlorophyll Index (CIg), the Structure Insensitive Pigment Index (SIPI), the Normalized Difference Water Index (NDWI), and the Visible Atmospherically Resistant Index (VARI). After experimentation, the VARI showed promising results. Throughout understanding the histogram, the masked VARI showed the dots related to the location of fruits, as shown in Figure 27. In the RGB composite, the fruit is the black and white dots surrounded the leaves, as displayed in Figure 28. Further research is needed to understand the reach for using thresholding for identifying fruits in dense plantations.

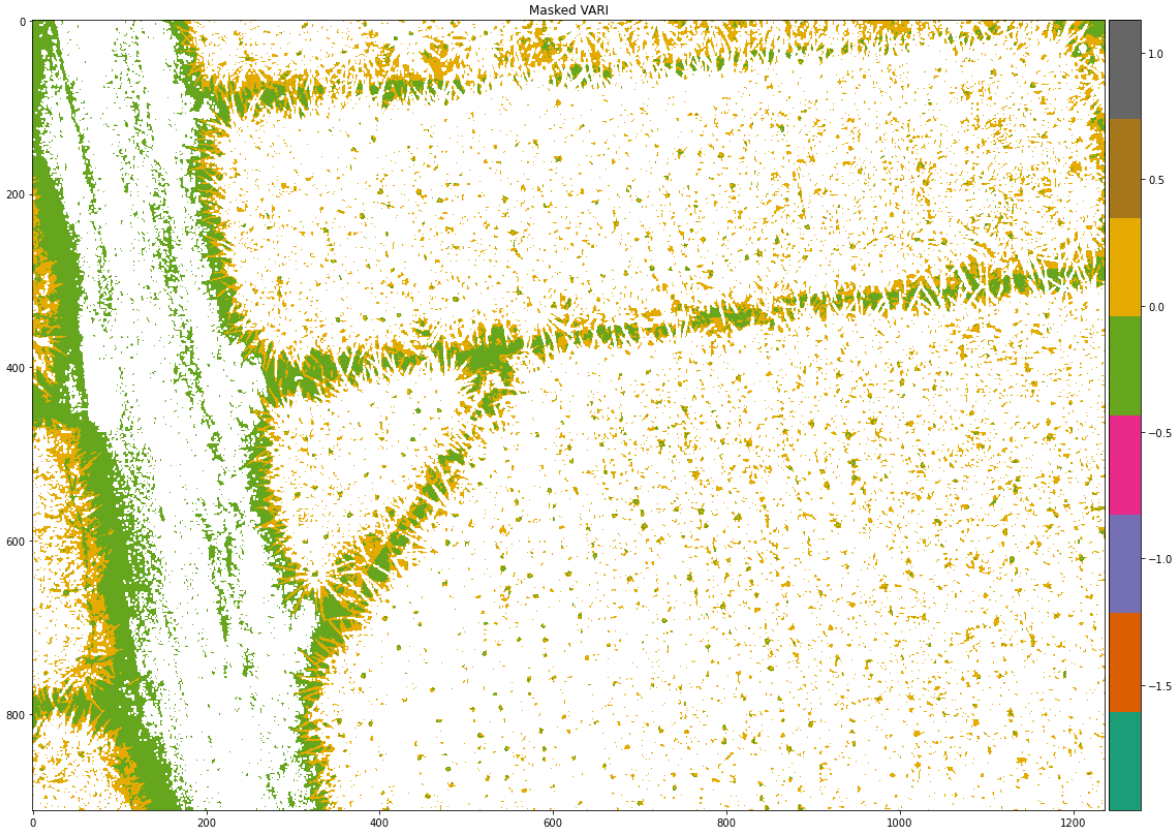

Figure 27 Masked VARI Isolated Pineapples

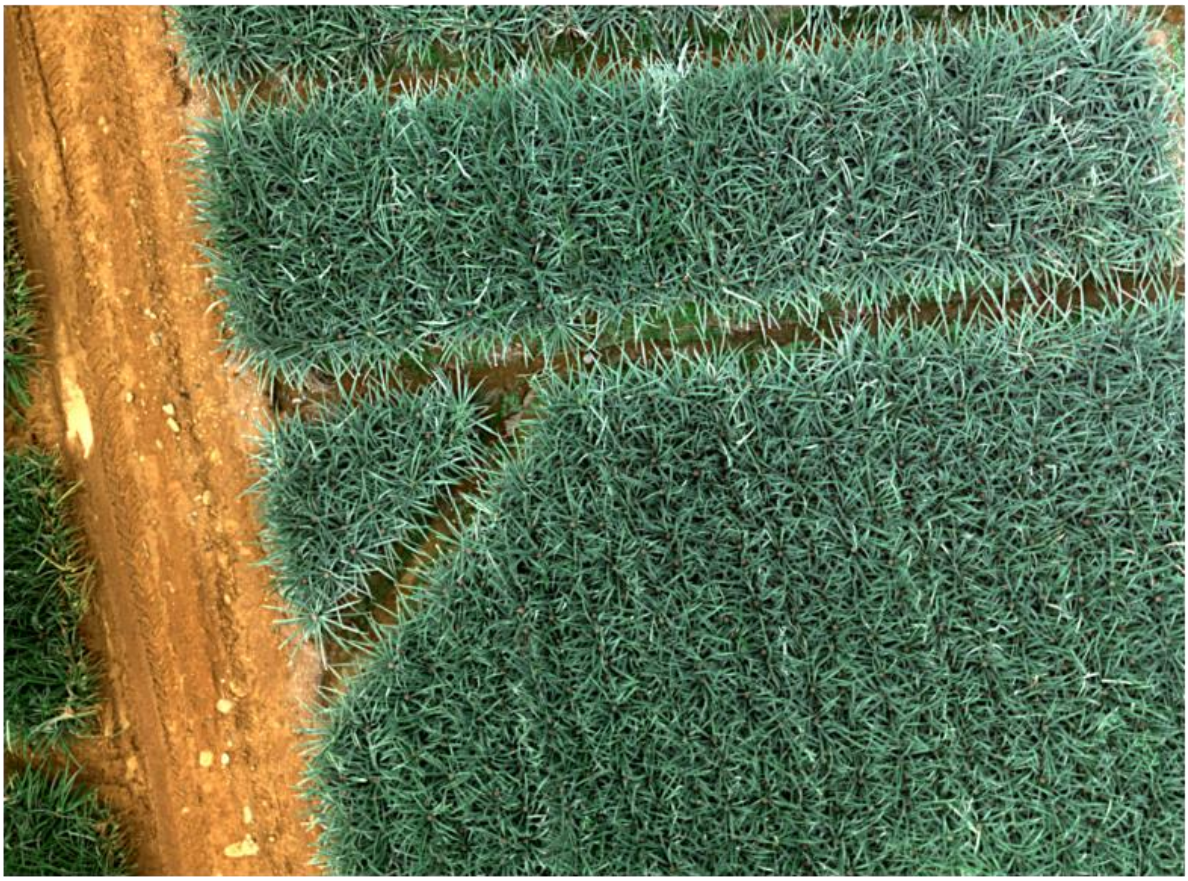

Figure 28 Pineapple 002 enhanced RGB Composite

5.2 Discussion

The blueberry and tequila agave datasets required heavy manual data cleaning. Since there was no data acquisition methodology, the captures contained objects which generated noise for the image analysis. Examples of the objects include shoes, jeans, and rocks. The code partially filtered the unwanted objects, but the downside was that it also removed some ROI pixels. External objects make it harder to segment crops and fruits from other pixels. Third, the crop images should be captured far away from white objects. White objects generate distortion in the band-to-band alignment process and cause problems filtering them out. Fourth, the white labels and the white tube hindered results and plant categorization because they hid leaves and branches. Fifth, the blueberry dataset contained captures with only four TIFF files instead of five.

The Pineapple Plantation dataset was captured at an altitude of more than 30 meters and using the knowledge acquired from the previous dataset. It contained duplicates, but the number of

issues was significantly less. The dataset contained a few captures, so the orthomosaic map was not created. Further research is needed to understand the reach for using thresholding for identifying fruits in dense plantations. Nonetheless, the NDVI and NDRE successfully segmented the crops from the background using thresholding.

The data acquisition methodology is critical to reducing noise in image analysis. A correct data acquisition methodology includes capturing panel images before and after the flight. The panel should be placed flat on the ground and away from objects affecting lighting conditions. They are critical for radiometric calibration. Moreover, the time of day for capturing data is essential. Captures should be taken within two and a half hours of local solar noon. In case the day is very sunny, fly while the sun is at an angle lower than 90 degrees. In the case of cloudy days, the sun may partly obscure sections of the images. Finally, images should be taken with the same sequence or planning route on different days.

6. CONCLUSIONS

The range in topography, biodiversity, and agricultural technology has led to the emergence of precision agriculture. In precision agriculture, computer vision, image analysis, and image processing are gaining considerable traction. For this work, image analysis involves recognizing individual objects and providing insights from an image. For image analysis, vegetation indices were implemented using thresholding to segment plants and fruits from the background. The data acquired was remote-sensed multispectral images from blueberry, maguey, and pineapple. The studied crops have a high market share in Mexico´s agriculture production and exports.

In the State of Art section, the study summarizes applications and aspects of remotely sensed images in precision agriculture. The data source can be RGB, multispectral, hyperspectral, and 3D images. Applications include fruit and plant detection, grading and counting fruits, leaf disease detection, quality characterization, crop yield prediction, and field inspection. In the Theoretical Framework section, the research compiles the concepts for acquiring, processing, and analyzing remote-sensed multispectral images. The main concepts are spectral bands, spatial resolution, radiometric resolution, radiometric calibration, spectral signature, and vegetation indices. Radiometric calibration allows researchers to compare and contrast data captured over different days or at different times. The two levels of radiometric calibration involved converting an image's raw digital pixel values to spectral radiance and then from spectral radiance to surface reflectance values.

The Methodology section describes the blueberry, tequila agave, and pineapple datasets and the economic importance of the crops. While the blueberry and tequila agave datasets contain single captures of plants on pots at low altitudes, the pineapple dataset has images from a nine-week-old plantation. Moreover, the processing flow guides and explains the radiometric calibration and image alignment using the custom code from the MicaSense repository. It was built using open-source tools including python, OpenCV, Matplot, Numpy, and more. At the start of the research, custom algorithms and libraries were coded to read and process images using OpenCV, Pandas, and Numpy. After the MicaSense repository was found and

checked, it was a perfect match to use for the implementation of a methodology to process and analyze multispectral images using vegetation indices.

The Results section presents insights from the RGB composites and vegetation indices. A fundamental finding is that the methodology for acquiring data affected the image post-processing. The blueberry and tequila agave captures contained objects which generated noise, such as shoes, jeans, white labels, white tubes, and rocks. The code partially filtered the unwanted objects, but the downside was that it also removed plant pixels. Furthermore, external objects make it harder to segment crops and fruits from other pixels when they have a similar spectral signature.

The four leading vegetation indices used were the Normalized Difference Vegetation Index (NDVI), the Normalized Difference Red Edge (NDRE), the Simple Ratio, the Red Edge Chlorophyll Index, and the Visible Atmospherically Resistant Index (SAVI). After computing vegetation indices, histograms were analyzed to choose thresholds. The masking of vegetation indices with threshold allowed the removal of areas with shadows and soil. The NDVI was particularly useful for removing soil pixels. So it was used as a baseline to soil from other vegetation indices. Moreover, the NDVI and NDRE were the most useful for segmenting the background from the crops. There is no formula for identifying fruits; vegetation indices should be tested and analyzed.

The top leadership group of Precisión Agrícola was closely involved with this work. A valuable outcome of this endeavor is a series of good practices and recommendations that Precisión Agrícola can apply to its methodology for acquiring and analyzing images. The most valuable recommendations include using radiometric calibration, capturing images at high altitudes (more than meters), removing unnecessary objects in the scene before capturing images, and using NDVI and NDRE to segment crops from the background. Undoubtedly, it contributes to its quest to achieve food safety for Mexico.

7. BIBLIOGRAPHY

[1] The Nationa Research Council, *Precision Agriculture in the 21st Century: Geospatial and Information Technologies in Crop Management*, 1997th ed. Washington DC: The National Academies Press. doi: 10.17226/5491.

[2] K. Navulur, *Multispectral Image Analysis Using the Object-Oriented Paradigm*, 0 ed. CRC Press, 2006. doi: 10.1201/9781420043075.

[3] A. M. Ali *et al.*, "Crop Yield Prediction Using Multi Sensors Remote Sensing (Review Article)," *The Egyptian Journal of Remote Sensing and Space Science*, p. S1110982322000527, May 2022, doi: 10.1016/j.ejrs.2022.04.006.

[4] M. K. Bhuyan, *Computer Vision and Image Processing: Fundamentals and Applications*. CRC Press, 2019.

[5] R. C. Gonzalez and R. E. Woods, *Digital image processing*. New York, NY: Pearson, 2018.

[6] C. S. Pereira, R. Morais, and M. J. C. S. Reis, "Recent advances in image processing techniques for automated harvesting purposes: A review," in *2017 Intelligent Systems Conference (IntelliSys)*, London, Sep. 2017, pp. 566–575. doi: 10.1109/IntelliSys.2017.8324352.

[7] X.-F. Wang and D.-S. Huang, "A Novel Multi-Layer Level Set Method for Image Segmentation," p. 25.

[8] E. Mavridou, E. Vrochidou, G. A. Papakostas, T. Pachidis, and V. G. Kaburlasos, "Machine Vision Systems in Precision Agriculture for Crop Farming," p. 32, 2019.

[9] F. Garcia-Lamont, J. Cervantes, A. López, and L. Rodriguez, "Segmentation of images by color features: A survey," *Neurocomputing*, vol. 292, pp. 1–27, May 2018, doi: 10.1016/j.neucom.2018.01.091.

[10] P. Sharma, P. Hans, and S. C. Gupta, "Classification Of Plant Leaf Diseases Using Machine Learning And Image Preprocessing Techniques," in *2020 10th International Conference on Cloud Computing, Data Science & Engineering (Confluence)*, Noida, India, Jan. 2020, pp. 480–484. doi: 10.1109/Confluence47617.2020.9057889.

[11] D. Choi, W. S. Lee, J. K. Schueller, R. Ehsani, F. Roka, and J. Diamond, "A performance comparison of RGB, NIR, and depth images in immature citrus detection using deep learning algorithms for yield prediction.," 2017. doi: 10.13031/aim.201700076.

[12] C. Yang, W. S. Lee, P. Gader, and H. Li, "Hyperspectral band selection using Kullback-Leibler divergence for blueberry fruit detection," in *2013 5th Workshop on Hyperspectral Image and Signal Processing: Evolution in Remote Sensing (WHISPERS)*, Gainesville, FL, USA, Jun. 2013, pp. 1–4. doi: 10.1109/WHISPERS.2013.8080640.

[13] C. Yang, W. S. Lee, and J. G. Williamson, “Classification of blueberry fruit and leaves based on spectral signatures,” *Biosystems Engineering*, vol. 113, no. 4, pp. 351–362, Dec. 2012, doi: 10.1016/j.biosystemseng.2012.09.009.

[14] L. Qi, X. Ma, Y. Zuo, X. Liao, and H. Guo, “Multispectral image segmentation of rice seedlings in paddy fields by fuzzy c-means clustering,” in *2010 3rd International Congress on Image and Signal Processing*, Yantai, China, Oct. 2010, pp. 1427–1430. doi: 10.1109/CISP.2010.5646677.

[15] A. M. de Oca, L. Arreola, A. Flores, J. Sanchez, and G. Flores, “Low-cost multispectral imaging system for crop monitoring,” in *2018 International Conference on Unmanned Aircraft Systems (ICUAS)*, Dallas, TX, Jun. 2018, pp. 443–451. doi: 10.1109/ICUAS.2018.8453426.

[16] S. Sabzi, Y. Abbaspour-Gilandeh, and H. Javadikia, “Machine vision system for the automatic segmentation of plants under different lighting conditions,” *Biosystems Engineering*, vol. 161, pp. 157–173, Sep. 2017, doi: 10.1016/j.biosystemseng.2017.06.021.

[17] A. J. Irias Tejeda and R. Castro Castro, “Algorithm of Weed Detection in Crops by Computational Vision,” in *2019 International Conference on Electronics, Communications and Computers (CONIELECOMP)*, Cholula, Mexico, Feb. 2019, pp. 124–128. doi: 10.1109/CONIELECOMP.2019.8673182.

[18] A. Lakshmanarao, M. R. Babu, and T. S. R. Kiran, “Plant Disease Prediction and classification using Deep Learning ConvNets,” in *2021 International Conference on Artificial Intelligence and Machine Vision (AIMV)*, Gandhinagar, India, Sep. 2021, pp. 1–6. doi: 10.1109/AIMV53313.2021.9670918.

[19] J. Deng, Z. Niu, X. Zhang, J. Zhang, S. Pan, and H. Mu, “Kiwifruit vine extraction based on low altitude UAV remote sensing and deep semantic segmentation,” in *2021 IEEE International Conference on Artificial Intelligence and Computer Applications (ICAICA)*, Dalian, China, Jun. 2021, pp. 843–846. doi: 10.1109/ICAICA52286.2021.9498221.

[20] S. Sengupta and W. S. Lee, “Identification and determination of the number of immature green citrus fruit in a canopy under different ambient light conditions,” *Biosystems Engineering*, vol. 117, pp. 51–61, Jan. 2014, doi: 10.1016/j.biosystemseng.2013.07.007.

[21] X. Ni, C. Li, H. Jiang, and F. Takeda, “Deep learning image segmentation and extraction of blueberry fruit traits associated with harvestability and yield,” *Hortic Res*, vol. 7, no. 1, p. 110, Dec. 2020, doi: 10.1038/s41438-020-0323-3.

[22] J. A. Richards, *Remote Sensing Digital Image Analysis: An Introduction*. Springer Science & Business Media, 2012.

[23] I. Amro, J. Mateos, M. Vega, R. Molina, and A. K. Katsaggelos, “A survey of classical methods and new trends in pansharpening of multispectral images,” *EURASIP J. Adv. Signal Process.*, vol. 2011, no. 1, p. 79, Dec. 2011, doi: 10.1186/1687-6180-2011-79.

[24] S. Candiago, F. Remondino, M. D. Giglio, M. Dubbini, and M. Gattelli, “Evaluating Multispectral Images and Vegetation Indices for Precision Farming Applications from UAV Images,” p. 22, 2015.

[25] R. A. Schowengerdt, *Remote Sensing, Models, and Methods for Image Processing*. Academic Press, 1997.

[26] Yu Haiyang, Liu Yanmei, Yang Guijun, and Yang Xiaodong, “Quick image processing method of HJ satellites applied in agriculture monitoring,” in *2016 World Automation Congress (WAC)*, Rio Grande, PR, USA, Jul. 2016, pp. 1–5. doi: 10.1109/WAC.2016.7583037.

[27] S. Philip H. and D. Shirley M., *Remote Sensing: The Quantitative Approach*, W. C. Kennard., vol. 3. New York: McGraw-Hill International Book Co., 1978.

[28] J. Cavender-Bares, J. A. Gamon, and P. A. Townsend, Eds., *Remote Sensing of Plant Biodiversity*. Cham: Springer International Publishing, 2020. doi: 10.1007/978-3-030-33157-3.

[29] C. Zhang and J. M. Kovacs, “The application of small unmanned aerial systems for precision agriculture: a review,” *Precision Agric*, vol. 13, no. 6, pp. 693–712, Dec. 2012, doi: 10.1007/s11119-012-9274-5.

[30] N. G. Silleos, T. K. Alexandridis, I. Z. Gitas, and K. Perakis, “Vegetation Indices: Advances Made in Biomass Estimation and Vegetation Monitoring in the Last 30 Years,” *Geocarto International*, vol. 21, no. 4, pp. 21–28, Dec. 2006, doi: 10.1080/10106040608542399.

[31] G. M. Gandhi, S. Parthiban, N. Thummalu, and A. Christy, “Ndvi: Vegetation Change Detection Using Remote Sensing and Gis – A Case Study of Vellore District,” *Procedia Computer Science*, vol. 57, pp. 1199–1210, 2015, doi: 10.1016/j.procs.2015.07.415.

[32] S. S. Somvanshi and M. Kumari, “Comparative analysis of different vegetation indices with respect to atmospheric particulate pollution using sentinel data,” *Applied Computing and Geosciences*, vol. 7, p. 100032, Sep. 2020, doi: 10.1016/j.acags.2020.100032.

[33] B. Boiarskii, “Comparison of NDVI and NDRE Indices to Detect Differences in Vegetation and Chlorophyll Content,” *JMCMS*, vol. spl1, no. 4, Nov. 2019, doi: 10.26782/jmcms.spl.4/2019.11.00003.

[34] Q. Xie *et al.*, “Vegetation Indices Combining the Red and Red-Edge Spectral Information for Leaf Area Index Retrieval,” *IEEE J. Sel. Top. Appl. Earth Observations Remote Sensing*, vol. 11, no. 5, pp. 1482–1493, May 2018, doi: 10.1109/JSTARS.2018.2813281.

[35] J. Teng *et al.*, “Assessing habitat suitability for wintering geese by using Normalized Difference Water Index (NDWI) in a large floodplain wetland, China,” *Ecological Indicators*, vol. 122, p. 107260, Mar. 2021, doi: 10.1016/j.ecolind.2020.107260.

[36] Y. Zheng, L. Tang, and H. Wang, “An improved approach for monitoring urban built-up areas by combining NPP-VIIRS nighttime light, NDVI, NDWI, and NDBI,” *Journal of Cleaner Production*, vol. 328, p. 129488, Dec. 2021, doi: 10.1016/j.jclepro.2021.129488.

[37] M. Mokarram, A. D. Boloorani, and M. Hojati, “Relationship between land cover and vegetation indices. Caste Study: Eghlid plain, fars province, Iran,” vol. 7, no. 2, p. 13, 2016.

[38] “Food and Agricultural Overview 2019,” Food, Agricultural and Fisheries Information Service (SIAP), Mexico, Government 1, 2019. Accessed: November 17, 2020. [Online]. Available: https://nube.siap.gob.mx/gobmx_publicaciones_siap/pag/2019/Agricultural-Atlas-2019

[39] F. de J. G. Razo, S. R. Rebollar, J. H. Martínez, J. L. M. Hernández, and O. R. Abarca, “SITUACION ACTUAL Y PERSPECTIVAS DE LA PRODUCCIÓN DE BERRIES EN MÉXICO,” *Revista Mexicana de Agronegocios*, vol. 44, pp. 260–272, Jun. 2019, doi: 10.22004/ag.econ.292265.

[40] B. R. Gibson and D. T. Mitchell, “Nutritional influences on the solubilization of metal phosphate by ericoid mycorrhizal fungi,” *Mycological Research*, vol. 108, no. 8, pp. 947–954, Aug. 2004, doi: 10.1017/S095375620400070X.

[41] C. F. Scagel, “Inoculation with Ericoid Mycorrhizal Fungi Alters Fertilizer Use of Highbush Blueberry Cultivars,” *HortSci*, vol. 40, no. 3, pp. 786–794, Jun. 2005, doi: 10.21273/HORTSCI.40.3.786.

[42] A. K. Brody *et al.*, “Genotype-specific effects of ericoid mycorrhizae on floral traits and reproduction in *Vaccinium corymbosum*,” *Am J Bot*, vol. 106, no. 11, pp. 1412–1422, Nov. 2019, doi: 10.1002/ajb2.1372.

[43] Servicio de Información AgroAlimentaria y Pesquera (SIAP), “Panorama Agroalimentario 2021.” 2021. [Online]. Available: https://nube.siap.gob.mx/panorama_siap/pag/2021/Panorama-Agroalimentario-2021

[44] J. J. Coria-Contreras *et al.*, “Epidemiología regional aplicada a la caracterización inductiva y pronóstico de la mancha gris del agave azul (Cercospora agavicola) en Jalisco, México,” *RMF*, vol. 37, no. 1, Dec. 2018, doi: 10.18781/R.MEX.FIT.1809-4.

[45] “Food and Agricultural Overview 2021,” Food, Agricultural and Fisheries Information Service (SIAP), Mexico, Government, 2021. [Online]. Available: https://nube.siap.gob.mx/panorama_siap/pag/2021/Agricultural-Atlas-2021